



Norwegian University of
Science and Technology

Identification of Material Properties of an Aluminium Alloy

Marie Nordhaug

Civil and Environmental Engineering

Submission date: June 2017

Supervisor: Tore Børvik, KT

Co-supervisor: Susanne Thomesen, KT
Egil Fagerholt, KT

Norwegian University of Science and Technology
Department of Structural Engineering



MASTER THESIS 2017

SUBJECT AREA: Computational Mechanics	DATE: June 11, 2017	NO. OF PAGES: 8 + 72 + 3
--	------------------------	-----------------------------

TITLE:

Identification of Material Properties of an Aluminium Alloy

BY:

Marie Nordhaug



SUMMARY:

Uniaxial tension tests of small versus large round specimens and small versus large flat specimens from a 3XXX series aluminium alloy were carried out to identify the mechanical properties of the material. Different measurement techniques such as laser micrometer, edge tracing and Digital Image Correlation (DIC) were applied in the tests. In addition, extensometers were used to validate the results from the edge-trace and DIC approaches. The results from the tension tests were processed and the true stress-strain curves were obtained. For the round specimens, the data were measured all the way to fracture while for the flat specimens the measured data were only evaluated until diffuse necking. The results showed good agreement within each specimen geometry and measurement technique. A deviation between the small round specimen and the three other specimen geometries was observed in the comparison of the round and flat specimens.

Based on the experimental results the material constants in the modified Johnson-Cook (MJC) constitutive relation were calibrated. The measured data from the flat tension tests had to be extrapolated from diffuse necking. The method of extrapolation was discussed and, depending on the hardening laws, the extrapolation gave different material behaviour at large plastic strains. This showed that the method of extrapolation is only an approximation that could lead to an incorrect material behaviour in complex nonlinear structural problems.

Fracture was not evaluated in this thesis, hence ABAQUS/Standard was used in the numerical work. Simulations of the tension tests based on the direct calibration were performed and the results corresponded with the experimental results, hence the direct calibration predicted the material behaviour well in this case. The material parameters in the MJC constitutive relation were optimized using inverse modelling in LS-OPT. Compared with the experimental results, the optimization gave a very good fit for the flat specimens, while it resulted in a lower stress level at large plastic strains for the round specimens.

Finally, a numerical case study was performed to investigate that the material properties obtained from the round and flat tension tests gave the same result in a nonlinear finite element simulation. The study showed that the material data from the round and flat specimens resulted in approximately the same material behaviour in a complex nonlinear problem with large plastic strains in this case. This demonstrated that the round and flat tensile specimens were both valid to identify mechanical properties of materials.

RESPONSIBLE TEACHER: Professor Tore Børvik

SUPERVISOR(S): Professor Tore Børvik, PhD Candidate Susanne Thomesen and PhD Egil Fagerholt

CARRIED OUT AT: SIMLab, The Department of Structural Engineering, NTNU



MASTEROPPGAVE 2017

FAGOMRÅDE: Beregningsmekanikk	DATO: 11.juni 2017	ANTALL SIDER: 8 + 72 + 3
----------------------------------	-----------------------	-----------------------------

TITTEL:

Identifisering av materialegenskaper til en aluminiumslegering

UTFØRT AV:

Marie Nordhaug



SAMMENDRAG:

Enaxial stresstester av små mot store runde prøvestykker og små mot store flate prøvestykker fra en 3XXX serie aluminiumlegering var utført for å identifisere de mekaniske egenskaper til materialet. Ulike måleteknikker som laser mikrometer, edge-trace og Digital Image Correlation (DIC) var brukt i testene. I tillegg, ekstensometre ble brukt til å validere resultatene fra edge-trace og DIC metodene. Resultatene fra strekktestene var behandlet og den sanne spennings- og tøyningkurven ble funnet. For de runde prøvestykkene, dataene var målt helt fram til brudd mens for de flate prøvestykkene de målte dataene er kun vurdert til necking. Resultatene viste godt samsvar innen hver geometri og måleteknikk. Et avvik mellom det lille runde prøvestykket og de andre tre geometriene ble observert i sammenligningen mellom edge-trace og DIC metodene.

Basert på de eksperimentelle resultatene ble material konstantene i den modifiserte Johnson-Cook (MJC) konstitutiv relasjonen kalibrert. De målte dataene fra de flate prøvestykkene måtte ekstrapoleres fra necking. Ekstrapoleringsmetoden ble diskutert og, avhengig av fastingsregel, ekstrapoleringen ga forskjellig materialoppførsel ved store plastiske tøyninger. Dette viste at ekstrapoleringsmetoden er en tilnærming som kan føre til feil materialoppførsel i komplekse ikke-lineære konstruksjonsproblemer.

Brudd ble ikke vurdert i denne oppgaven, derfor ble ABAQUS/Standard brukt i det numeriske arbeidet. Simuleringer av strekktesten basert på direktekalibreringen var utført og resultatene stemte overens med de eksperimentelle resultatene som betyr at direkte kalibreringen forutså riktig materialoppførsel i dette tilfellet. Materialparameterne i MJC konstitutiv relasjon ble optimalisert ved bruk av inverse modellering i LS-OPT. Sammenlignet med de eksperimentelle resultatene, optimaliseringen ga en veldig god tilnærming for de flate prøvestykkene, men resulterte i et lavere spenningsnivå ved store plastiske tøyninger for de runde prøvestykkene.

Til slutt, et numerisk studium ble utført for å utforske om de mekaniske egenskapene oppnådd fra de runde og flate strekktestene ga det samme resultatet i ikke-lineære elementmetode simuleringer. Dette studiet viste at de oppnådde material dataene fra de runde og de flate prøvestykkene resulterte i cirka den samme materialoppførsel i et komplekst ikke-lineært problem med store plastiske tøyninger i dette tilfelle. Dette viste at de runde og de flate strekk-prøvestykkene var begge gyldige til å identifisere de mekaniske egenskaper til materialer.

FAGLÆRER: Professor Tore Børvik

VEILEDER(E): Professor Tore Børvik, ph.d kandidat Susanne Thomesen og forsker Egil Fagerholt

UTFØRT VED: SIMLab, Institutt for konstruksjonsteknikk, NTNU

MASTER'S THESIS 2017

for

Marie Nordhaug

Identification of Material Properties of an Aluminium Alloy

1. INTRODUCTION

The uniaxial tension test is by far the most used material test to provide information on the mechanical properties of metallic materials requested for finite element simulations. Traditionally, it also serves as an acceptance test for the specification of materials. In the tension test, a specimen is subjected to a continually increasing uniaxial tensile force while simultaneously observing the elongation of the gauge area of the specimen. Based on these measurements an engineering stress-strain curve can be constructed, which forms the basis for a direct calibration of the material at hand. However, during the last decade advances in computer technology and digital cameras have made various optical field-measuring techniques increasingly popular for identification of material properties. One such method is digital image correlation (DIC), which is a full-field image analysis method based on grey-value digital images, that can determine the contour and the displacements of an object under loading in both two and three dimensions. If DIC is combined with FEM, a very powerful tool in obtaining optimised material properties based on rather simple material tests becomes available. The main objective of this master thesis project is to evaluate different measurement techniques in the identification of material properties based on standard uniaxial tension tests, and compare their accuracy.

2. OBJECTIVES

The primary objective of the research project is to investigate how different measurement techniques and specimen geometries affect the calibration of constitutive relations and failure criteria for nonlinear finite element simulations of structural problems.

3. A SHORT DESCRIPTION OF THE RESEARCH PROJECT

The main topics in the research project will be as follows:

1. The candidate will conduct a review of relevant literature concerning material testing, experimental methods involving optical measurement techniques, constitutive relations and failure criteria for large-scale finite element simulations and material behaviour where the focus should be on aluminium alloys.
2. The candidate will carry out material tests on various specimens made from typical aluminium alloy. The material test program will involve small versus large axisymmetric (round) specimens, and small versus large dogbone (flat) specimens. During testing both a laser-scan micrometer, edge tracing and DIC will be used to measure the displacement.
3. Finite element models of all material specimens will be made in Abaqus, and sensitivity studies are carried out.
4. Various calibration methods should be considered to check if the material data do not change with calibration method and specimen type. This involves direct calibrations, inverse modelling using trial and error or LS-OPT, and combining DIC and FEM. The calibrated material models should be validated against each other in numerical simulations of some typical structural component.

Supervisors: Tore Børvik, Susanne Thomesen and Egil Fagerholt.

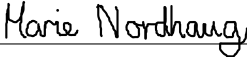
The thesis must be written according to current requirements and submitted to Department of Structural Engineering, NTNU, no later than June 11th, 2017.

NTNU, January 15th, 2017

Preface

This thesis was written in the spring of 2017 at the Structural Impact Laboratory (SIM-Lab) for the FRIPRO Toppforsk project (FractAI), located at the Department of Structural Engineering at the Norwegian University of Science and Technology (NTNU). After a 5 year study on the master program Civil and Environmental Engineering, with specialization in Structural Engineering, this thesis was the final requirement for the degree of Master of Science at NTNU. While writing the thesis, I also took the subject TKT4135 Material Mechanics which gave me new knowledge of material mechanics and relevant background information for this thesis.

Trondheim
June 11, 2017


Marie Nordhaug

Acknowledgement

I would like to thank Trond Auestad, Senior Engineer at SIMLab, for carrying out all the quasi-static tension tests in the laboratory. Your precision and accuracy resulted in successful tests and the information you gave me about the test setups was very helpful.

I would further thank the Associated Professor David Morin for making the input files for running LS-OPT analyses and solving my problems. I will also thank PhD Torodd Berstad for helping me to find the errors in my analyses. The PhD Candidate Henrik Graunm provided two numerical models which saved me a lot of time. I am grateful for that help.

PhD Egil Fagerholt deserves a large amount of gratitude for teaching me how to use the in-house software eCorr to extract material data based on edge tracing and DIC. Using eCorr in processing of the experimental results has been an important part of this thesis and I appreciate all the help I got. In addition, during this spring, Fagerholt implemented a new feature in eCorr which I used to detect the radius of curvature in the necked region of the specimens. I am grateful for all the time you have put into helping me.

My supervisor, PhD Candidate Susanne Thomesen, deserves a huge thank for all the valuable guidance in my work. You have always been available when I needed you and your thorough feedback has been incredible helpful. I highly appreciate your knowledge and I am very grateful for all the time and effort you have put into helping me during this thesis.

Finally, I would like to thank my main supervisor, Professor Tore Børvik, for weekly meetings from the beginning. I appreciate your guidance and advises during the work on this thesis. Thanks for sharing your experience within the field and your theoretical knowledge with me. Especially thanks for answering my questions days and nights.

Abstract

Uniaxial tension tests of small versus large round specimens and small versus large flat specimens from a 3XXX series aluminium alloy were carried out to identify the mechanical properties of the material. Different measurement techniques such as laser micrometer, edge tracing and Digital Image Correlation (DIC) were applied in the tests. In addition, extensometers were used to validate the results from the edge-trace and DIC approaches. The results from the tension tests were processed and the true stress-strain curves were obtained. For the round specimens, the data were measured all the way to fracture while for the flat specimens the measured data were only evaluated until diffuse necking. The results showed good agreement within each specimen geometry and measurement technique. A deviation between the small round specimen and the three other specimen geometries was observed in the comparison of the round and flat specimens.

Based on the experimental results the material constants in the modified Johnson-Cook (MJC) constitutive relation were calibrated. The measured data from the flat tension tests had to be extrapolated from diffuse necking. The method of extrapolation was discussed and, depending on the hardening laws, the extrapolation gave different material behaviour at large plastic strains. This showed that the method of extrapolation is only an approximation that could lead to an incorrect material behaviour in complex nonlinear structural problems.

Fracture was not evaluated in this thesis, hence ABAQUS/Standard was used in the numerical work. Simulations of the tension tests based on the direct calibration were performed and the results corresponded with the experimental results, hence the direct calibration predicted the material behaviour well in this case. The material parameters in the MJC constitutive relation were optimized using inverse modelling in LS-OPT. Compared with the experimental results, the optimization gave a very good fit for the flat specimens, while it resulted in a lower stress level at large plastic strains for the round specimens.

Finally, a numerical case study was performed to investigate that the material properties obtained from the round and flat tension tests gave the same result in a nonlinear finite element simulation. The study showed that the material data from the round and flat specimens resulted in approximately the same material behaviour in a complex nonlinear problem with large plastic strains in this case. This demonstrated that the round and flat tensile specimens were both valid to identify mechanical properties of materials.

Contents

Preface	i
Acknowledgement	iii
Abstract	v
Contents	vi
1 Introduction	1
1.1 Background	1
1.2 State of the Art	2
2 Theory	5
2.1 Aluminium Alloys	5
2.2 The Tension Test	6
2.3 Constitutive Relations and Fracture Criteria	9
2.3.1 The Johnson-Cook Model	10
2.3.2 The Cockcroft-Latham Fracture Criterion	11
2.3.3 The Johnson-Cook Fracture Criterion	12
2.4 Experimental Measurement Techniques	12
2.4.1 Edge Tracing	13
2.4.2 Laser Micrometer	13
2.4.3 Digital Image Correlation	13
2.4.4 Extensometer	14
2.5 Nanostructure Model	14
3 Experimental Work	17
3.1 Material Description	17

3.2	Geometries	18
3.3	Test Setup	19
3.3.1	Edge Tracing	19
3.3.2	Laser Micrometer	20
3.3.3	DIC	20
3.3.4	Extensometer	21
3.4	Experimental Results	21
3.4.1	Displacement of the Cross-Head	21
3.4.2	Round Specimen L5	23
3.4.3	Round Specimen L40	27
3.4.4	Flat Specimen L20	29
3.4.5	Flat Specimen L50	31
3.5	Scanning Electron Microscope	33
3.6	Discussion	35
4	Material Models	39
4.1	Calibration of Material Model	39
4.1.1	Round Specimens	39
4.1.2	Flat Specimens	45
4.2	Calibration of Fracture Model	46
5	Numerical Work	47
5.1	Direct Calibration	47
5.1.1	Round Tension Tests	47
5.1.2	Flat Tension Tests	51
5.2	Inverse Modelling	55
5.3	DIC-FEM	59
6	Numerical Case Study: Component Test	61
7	Concluding Remarks	65
8	Further Work	67
	Appendices	73
A	Appendix	73
A.1	Initial Dimensions of the Tensile Specimens	73
A.2	Nominal Dimensions of the Component	75

1 | Introduction

1.1 Background

In today's society, materials are daily used in structural design of e.g. cars, buildings or small items like kitchen equipment. Reliable mechanical properties of materials are therefore extremely important to assure safety and to avoid structural collapse, which in the worst case can lead to human fatalities. To provide information about mechanical properties of materials, the uniaxial tension test is by far the most used material test and it serves as an acceptance test for specification of materials. Based on measurements from the tension test an engineering stress-strain curve can be calculated, which forms the basis for a direct calibration of the material at hand. The identified mechanical properties of materials are further used in nonlinear finite element simulations of structural problems, e.g. design of structures subjected to large plastic strains, creep, local or global buckling or other complex nonlinear structural problems.

The most commonly used tensile specimens are axisymmetric specimens with round cross-section and flat specimens with dog-bone shaped cross-section. From tension tests of round specimens the experimental data are measured all the way to fracture, while for flat specimens the measured data are only valid until diffuse necking and extrapolation is necessary in order to obtain data all the way to fracture. Due to limitations in the geometry of some structural designs (e.g. use of thin plates in the car industry), only the flat tensile specimens can be used to identify the material properties in some applications.

In a uniaxial tension test, the elongation of the tensile specimen is traditionally measured with an extensometer. However, advances in computer technology and digital cameras during the last decades have made various optical measuring techniques available for identification of material properties. One such method is Digital Image Correlation (DIC), which is a non-contact optical method for measuring displacement fields of specimens. However, limitations in time and equipment often lead to the use of extensometers instead of more advanced optical methods such as DIC.

The main objective of this thesis is to investigate the reliability of the material properties identified from uniaxial tension test of small versus large flat specimens compared with small versus large round specimens, manufactured from the same aluminium alloy. Uniaxial tension tests will be performed on all four specimen geometries, where different measurement techniques such as laser micrometer, DIC and edge tracing will be used to

measure displacements. The experimental data will further be numerically analysed and validated using ABAQUS/Standard in order to check if the material data do not change with calibration method and specimen type. Finally, the experimental data will be used in a numerical case study to investigate if the different material input data have an effect on the result in a complex nonlinear structural problem.

1.2 State of the Art

Throughout ancient history, the knowledge of the materials ability to sustain a load before breaking has been of great importance since structures were first built. Early stages of development of methods and test machines for determination of the strength of materials started from approximately the 16th century [1]. Reliable tensile data are crucial in design of safe structures since unreliable data can cause catastrophic failure leading to human fatalities. By the 19th century the importance of tension testing of metallic materials was undertaken in the UK and one of the earliest British Standards (BS18), covering the subject, was published in 1904. In 1938, BS18 was revised with specification of the test method, not only the test pieces, and today the European Tensile Testing Standard (first published in 1990) has superseded the BS18. During the last decades, the uniaxial tensile test has become the primary method for identification of material properties. There exist numerous articles, books and manuals about tension testing, where e.g. [2, 3, 4] provide thorough summaries of research within the field. One of the latest books, published in 2004 by Davis [5], gives a complete review of the theory, procedure and application of the tension test.

Mechanical testing machines have been commercial available since 1886 [6]. Since then, the evolution has gone from purely mechanical machines to hydraulic machines with advanced electronics and microcomputers. Today, universal testing machines (UTM) have the capability to test materials in tension, compression and bending. In tension testing, the displacement of the specimen can be measured in several ways. Extensometers are one of the traditional strain gauges and go back to mid 19th century. The notable extensometers were Hodgkinson's wedge gauge and Unwin's tough micrometer, in addition to the well-known dial indicator from 1890 [7]. Today, the extensometers are widely used devices and can provide a high degree of measurement accuracy. The various types of extensometers are thoroughly described by e.g. House and Gillis [6]. In the sixties, the first laser was demonstrated and the laser beams were later adapted to mechanical testing. In 1966, a classical review paper was published by Kogelnik and Li [8], which became the standard reference on the description of the laser beams for many years. The laser beams made it possible to perform non-contact measurements of specimens and were a technological advance within the field. Since their publication, a lot of research has been conducted and many advances have occurred. The latest review on the topic is the *Handbook of Optical and Laser Scanning* published by Marshall and Stutz in 2011 [9].

A repeating problem with the existing measurement techniques is the difficulty of doing measurements outside the laboratory. There is a balance between accuracy, ease of use and costs that must be satisfied. However, during the last decades advances in

both computer technology and digital cameras have made various optical field measuring techniques increasingly popular for identification of material properties. Digital Image Correlation (DIC) is a non-contact optical measurement technique for determining the surface deformation of specimens. The method is cost efficient and in general simple to use [10]. The development of DIC started in the 1980s [11]. Since then, the technology has been improved through research in order to increase the resolution and to improve the accuracy. In the early 2000s, Hild and Roux [12, 13] studied how the DIC technique could be used to identify material properties. The research showed to be very accurate and, especially for brittle materials, the technique appeared as extremely appealing. Generally, the DIC method have enhanced both the accuracy of the displacement estimated and the reliability of the identification of mechanical properties [12, 13]. A recent article regarding full-field measurement was published by Marth et al. [14] in 2016. The article compares the method of stepwise modelling using DIC with inverse modelling, a method introduced by Zhano and Li [15] in 1994. Marth et al. [14] concluded that the optical full-field displacement measurements can be used to calculate a local strain field and that the stepwise modelling method with DIC is considerably faster compared with inverse modelling.

Fagerholt [16] developed the in-house DIC software eCorr in 2012 used in this thesis. The software connects the measured displacement field with the DIC algorithm and hence, the strain-field may be obtained. The software is a powerful tool and has since its development been widely used for in-house experiments. Edge tracing is another feature that is implemented in eCorr. Edge tracing is an optical measurement technique, where the latest technique uses digital cameras together with software to detect the minimum diameter of axisymmetric specimens. The minimum diameter has previously been measured using lasers, but as the technology and digital cameras have been developed, the method has been simplified and got a wider area of applications. A description of the use of edge tracing with optical techniques is proposed by Kristensen et al. [17].

Through the decades the different measurement techniques have been thoroughly described in the literature. However, the different methods are rarely compared in the same experiment with various specimens from the same material in order to investigate the result. In this thesis, uniaxial tension tests are performed on four different specimen geometries from an aluminium alloy of the 3XXX series with the use of different measurement techniques are investigated. The different methods are compared, and parameters such as accuracy and user-friendliness are evaluated. This investigation will hopefully provide insight on how the different measurement techniques affect the result, in addition to give an understanding of the user-friendliness for an untrained user.

2 | Theory

2.1 Aluminium Alloys

Aluminium alloys are lightweight metals with a wide range of applications. Compared to other metals such as steel, aluminium possesses substantial advantage in weight reduction for structural components (2.7 g/m^3 density compared to 7.83 g/m^3 for iron). Pure aluminium is soft, ductile and has a high electrical conductivity, in addition to ease of fabrication and appearance. However, in order to secure adequate mechanical strength in many engineering applications, aluminium has to be alloyed and also, very often, heat treated.

Aluminium alloys are classified into a four-digit numbering system, where the first digit indicates the major alloying element. From Schweitzer et al. [18] the classification of aluminium alloys is as shown in Table 2.1. Note that all the alloy classes in Table 2.1 contain other minor alloying elements.

Table 2.1: Classification of aluminium alloys [18].

Series designation	Major alloying element
1XXX	Aluminium > 99.0 %
2XXX	Copper
3XXX	Manganese
4XXX	Silicon
5XXX	Magnesium
6XXX	Magnesium and silicon
7XXX	Zinc
8XXX	Other elements
9XXX	Unused series

Wrought alloys are subdivided into their ability of being heat treated or not. Wrought alloys that are non-heat treatable must be strengthened by strain hardening and are designated the letter H. These alloys are in the 1XXX, 3XXX, 4XXX and 5XXX series. In general, the non-heat treatable alloys have a high resistance to corrosion. On the other hand, the heat treatable alloys are of the 2XXX, 6XXX and 7XXX series and are designated the letter T. When it comes to cast aluminium, there is no single commercial

designation system. However, as for wrought aluminium, cast aluminium is classified as heat treatable and non-heat treatable alloys. In addition to strain hardening and heat treatment, all alloys can be cold worked to increase strength [18]. The degree of increased strength depends on the alloy class.

2.2 The Tension Test

The uniaxial tension test is by far the most used material test to provide information of the mechanical properties of materials and is an acceptable test for characterisation of materials. The following process of extracting material properties from the tension test is based on Hosford and Caddell [4].

In a tension test a specimen is subjected to a continually increasing uniaxial tensile force while simultaneously observing the elongation of the gauge region of the specimen. The *nominal* or *engineering stress*, σ_e , and *strain*, ε_e , are based directly on the measurements of the tensile force, F , and the elongation, ΔL , of the specimen. The engineering stresses and strains are defined as

$$\sigma_e = \frac{F}{A_0}, \quad \varepsilon_e = \frac{\Delta L}{L_0} = \frac{L - L_0}{L_0} \quad (2.1)$$

where A_0 is the initial cross-sectional area and L_0 is the initial gauge length of the specimen. Since both A_0 and L_0 are constant factors, the load-elongation curve will have the same shape as the engineering stress-strain curve.

When performing a tension test on metals the dimensions of the specimen change continuously during the test. As the specimen elongates, the cross-sectional area of the gauge length decreases uniformly until maximum load is reached. At maximum load, also referred to as the *tensile strength*, the cross-sectional area decreases rapidly and necking occurs. Since the engineering stresses and strains are based on the initial dimensions of the specimen, they will not give a true indication of the deformation of the specimen. To be able to extract the true mechanical properties of metals, the *Cauchy stress*, σ_t , and *logarithmic strain*, ε_l , need to be established.

The logarithmic strain, also referred to as the true strain, is based on instantaneous measurements of the incremental strain and from integration the logarithmic strain reads

$$\varepsilon_l = \int_{L_0}^L \frac{dL}{L} = \ln \frac{L}{L_0} = \ln(1 + \varepsilon_e) \quad (2.2)$$

where L is the current gauge length. The relationship between logarithmic and engineering strains is given in Equation 2.2. For metals and alloys the density changes measured after large plastic strains are less than 0.1 percentage and a good approximation is therefore that the volume remains constant during plastic deformation. Assuming volume preservation $A_0 L_0 = AL$, Equation 2.2 can be written in terms of either length or area, i.e.,

$$\varepsilon_l = \ln \frac{L}{L_0} = \ln \frac{A_0}{A} \quad (2.3)$$

where A is the current cross-sectional area of the specimen. Note that due to the assumption of volume preservation and a homogeneous distribution of strain along the gauge length of the specimen, the relationship between the logarithmic and engineering strains given in Equation 2.2 is only applicable to the onset of necking.

The Cauchy stress, also referred to as the true stress, is the tensile force at any instant divided by the current cross-sectional area of the specimen

$$\sigma_t = \frac{F}{A} \quad (2.4)$$

By the assumption of volume preservation, Equation 2.4 for the true stresses can be rewritten to a function of engineering stresses and strains as

$$\sigma_t = \frac{FL}{A_0L_0} = \sigma_e \frac{L}{L_0} = \sigma_e(1 + \varepsilon_e) \quad (2.5)$$

Note that Equation 2.5 is only valid until onset of necking due to the assumptions mentioned above. After necking, Equation 2.4 is used to calculate the true stresses.

Necking begins at maximum load during tensile deformation of a ductile material. Here, the increase in stress due to decrease in the cross-sectional area of the specimen becomes greater than the increase in the load-carrying ability of the metal due to strain hardening. This condition will be reached first at some point in the specimen that is slightly weaker than the rest. Necking is defined by $dF = 0$, or $d\sigma_e = 0$, and the diffuse necking criterion can be derived as following:

$$\begin{aligned} dF &= 0 \\ d(\sigma_t A) &= Ad\sigma_t + \sigma_t dA = 0 \Rightarrow d\sigma_t = -\frac{dA}{A}\sigma_t \end{aligned} \quad (2.6)$$

From the assumption of volume preservation $dV = 0$

$$d(AL) = LdA + AdL = 0 \Rightarrow \frac{dA}{A} = -\frac{dL}{L} = -d\varepsilon_l \quad (2.7)$$

By combining Equations 2.7 and 2.6, the diffuse necking criterion becomes

$$\frac{d\sigma_t}{d\varepsilon_l} = \sigma_t \quad (2.8)$$

The necking criterion, also known as the Considère criterion, is shown graphically in Figure 2.1

The phenomenon of necking can be divided into two types of tensile instabilities depending on the geometry of the specimens. For cylindrical specimens necking is symmetrical around the tensile axis if the material is isotropic. This type of instability is called diffused necking. For a sheet tensile specimen, where the width is much greater than the thickness, a second instability occurs. First the neck is analogous as for cylindrical specimen. This diffuse necking is followed by a second process where the neck is a narrow band

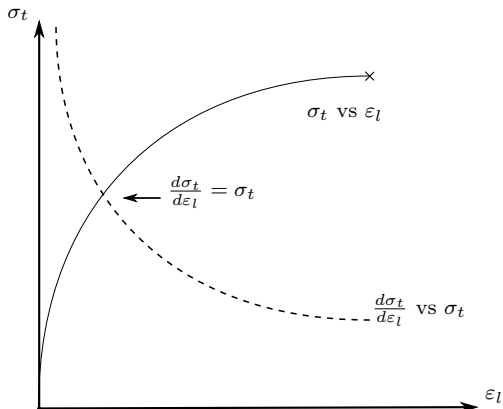


Figure 2.1: Graphical illustration of necking criterion. The black x marks the point of failure. Adapted from Hopperstad and Børvik [19].

with a width about equal to the sheet thickness inclined at an angle of the specimen's longitudinal axis. This second instability is called localized necking.

Beyond maximum load the cross-sectional area of the specimen is decreasing more rapidly than the deformation load is increased by strain hardening and the actual load required to deform the specimen falls off. The true stress-logarithmic strain curve is frequently linear from maximum load to fracture, while in other cases its slope continuously decreases up to fracture.

Ductile Fracture

Ductile fracture occurs as the result of nucleation, growth and coalescence of microscopic voids. Microvoids nucleate at inclusions and second-phase particles. The voids grow together to form a macroscopic flaw, which leads to fracture.

The commonly observed stages in ductile fracture are described as the following in Anderson [20]. A void forms around a second-phase particle or inclusion when the applied stress is sufficient to break the interfacial bonds between the particle and the matrix. Voids can also be nucleated when particles crack. Larger particles are more likely to crack in the presence of plastic strain, because they are more likely to contain small defects. Once the voids are formed they continue to grow due to plastic strain and hydrostatic stress, until they eventually coalesce with adjacent voids. Ductile fracture occurs when the voids reach a critical size, relative to their spacing, and a plastic instability produces a band of localized deformation. Figure 2.2 illustrates the growth and coalescence of microvoids in ductile materials.

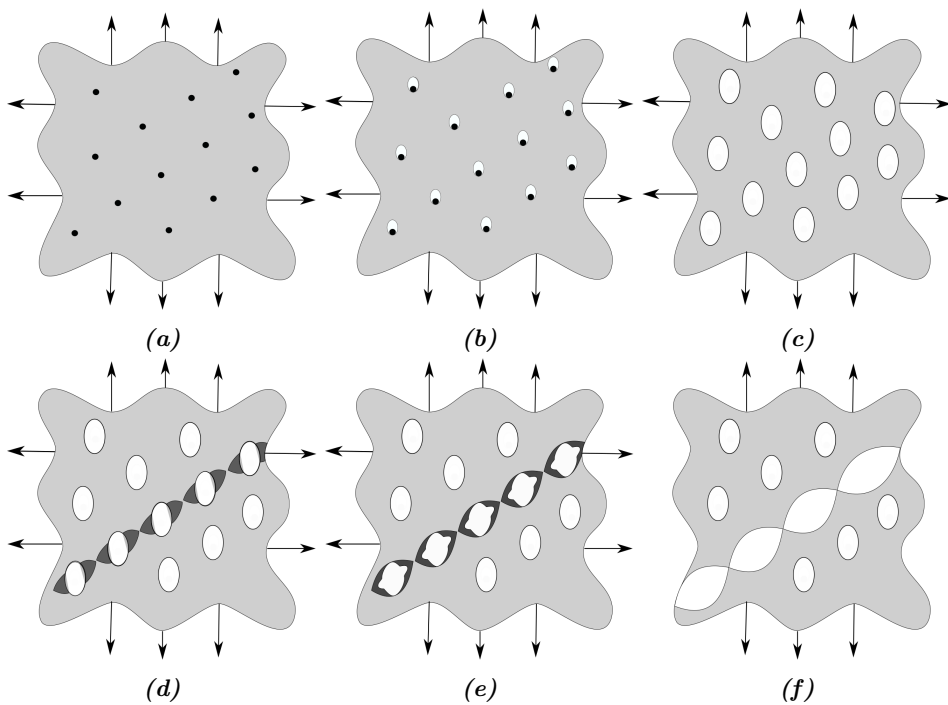


Figure 2.2: (a) Inclusions in a ductile matrix, (b) void nucleation, (c) void growth, (d) strain localization between voids, (e) necking between voids, (f) void coalescence and fracture. The figure is adapted from Andersen [20].

2.3 Constitutive Relations and Fracture Criteria

Constitutive relations describe the relation between stresses and strains in terms of the variables strain rate and temperature. A classic example of a constitutive relation is Hooke's law, which relates the stresses and strains of a linear elastic material during loading. Hooke's law is given as

$$\sigma = E\varepsilon \quad (2.9)$$

where σ is the stress, E is the Young's modulus and ε is the elastic strain. In impact mechanics, more advanced material models are required to describe e.g. material nonlinearities, strain-rate dependency and temperature dependency. One such material model is the Johnson-Cook (JC) model described in Section 2.3.1.

The constitutive relations do not predict material fracture. To predict fracture a fracture criterion is needed. Two well-used fracture criteria are the Cockcroft-Latham (CL) and the Johnson-Cook fracture criteria, which are described in Sections 2.3.2 and 2.3.3, respectively.

2.3.1 The Johnson-Cook Model

Johnson and Cook [21] presented in 1983 a constitutive model of thermo-viscoplasticity, which included the effects of strain hardening, strain rate hardening and thermal softening. The model is valid for isotropic materials and is applicable for materials subjected to large strains, high strain rates and high temperatures.

Assuming isotropic hardening, the yield function is defined as

$$f(\boldsymbol{\sigma}, R, T) = \varphi(\boldsymbol{\sigma}) - (\sigma_0(T) + R(p, T)) \quad (2.10)$$

where T is the current temperature and p is the equivalent plastic strain. The von Mises equivalent stress σ_{eq} , the yield stress σ_0 and the isotropic hardening variable R are given as

$$\sigma_{eq} \equiv \varphi(\boldsymbol{\sigma}) = \sqrt{\frac{3}{2} \sigma'_{ij} \sigma'_{ij}}, \quad \sigma_0(T) = A(1 - T^{*m}), \quad R(p, T) = Bp^n(1 - T^{*m}) \quad (2.11)$$

where σ'_{ij} is the deviatoric stress tensor, A , B , and n are material constants determining the work hardening and m defines the thermal softening. The homologous temperature T^* is defined as

$$T^* = \frac{T - T_r}{T_m - T_r} \quad (2.12)$$

where T_r is the reference temperature and T_m is the melting temperature of the material.

In the viscoplastic domain the yield function f equals the viscous stress σ_ν , i.e. $f(\boldsymbol{\sigma}, R, T) = \sigma_\nu(\dot{p}, p, T) > 0$. An alternative form of the von Mises equivalent stress is given as

$$\sigma_{eq} = \sqrt{\frac{3}{2} \sigma'_{ij} \sigma'_{ij}} = \sigma_0(T) + R(p, T) + \sigma_\nu(\dot{p}, p, T) \quad \text{for } f > 0 \quad (2.13)$$

where \dot{p} is the equivalent plastic strain rate. The viscous stress controls the strain rate sensitivity of the material and a multiplicative constitutive relation for this strain rate dependent is given as

$$\dot{p} = \dot{p}_0 \left[\left(\frac{\sigma_{eq}(\boldsymbol{\sigma})}{\sigma_0(T) + R(p, T)} \right)^{\frac{1}{C}} - 1 \right] \quad \text{for } f > 0 \quad (2.14)$$

where C is a material constant and \dot{p}_0 is a reference plastic strain rate. By solving Equation 2.14 for the equivalent stress, the constitutive relation for thermo-viscoplasticity reads

$$\sigma_{eq} = (A + Bp^n)(1 + \dot{p}^*)^C(1 - T^{*m}) \quad (2.15)$$

which is known as the modified Johnson-Cook (MJC) model. The dimensionless plastic strain rate is given by $\dot{p}^* = \dot{p}/\dot{p}_0$. Originally, the Johnson-Cook (JC) model was given as

$$\sigma_{eq} = (A + Bp^n)(1 + C \ln \dot{p}^*)(1 - T^{*m}) \quad (2.16)$$

The two versions of the model give similar results, but in the original model the logarithmic term may result in unwanted effects if $\dot{p}^* < 1$. This problem is avoided in the MJC model. In the JC model the first term represents the stress as a function of strain, the second term considers the effect of strain rate hardening and the third term includes the effect of temperature softening. The material constants in the JC model are identified through material tests, e.g. data from tension tests over a range of strain rates and temperatures. The JC model is therefore purely empirical and is widely used in numerical computations.

The isotropic hardening variable R is defined by the equivalent plastic strain p in Equations 2.15 and 2.16. Two frequently used isotropic hardening laws are the Power law and the Voce rule. The Power law is defined as

$$R(p) = Bp^n \quad (2.17)$$

and hence, the strain hardening term in the JC model follows the Power law. If the Power law is replaced by the Voce rule defined as

$$R(p) = \sum_{i=1}^N R_i(p) = \sum_{i=1}^N Q_{Ri}(1 - \exp(-C_{Ri}p)) \quad (2.18)$$

the constitutive relation for the MJC model is expressed as

$$\sigma_{eq} = \left(\sigma_0 + \sum_{i=1}^N Q_{Ri}(1 - \exp(-C_{Ri}p)) \right) (1 + \dot{p}^*)^C (1 - T^{*m}) \quad (2.19)$$

where Q_R and C_R are hardening parameters and N is typically 1, 2 or 3. Note that the parameter A in Equations 2.15 and 2.16 is replaced by σ_0 in Equation 2.19.

In structural impacts, i.e. in cases of high plastic strain rate, it is reasonable to assume adiabatic conditions. The temperature change due to adiabatic heating is given by

$$\Delta T = \int_0^p \chi \frac{\sigma_{eq}}{\rho C_p} dp \quad (2.20)$$

where ρ is the material density, C_p is the specific heat of the material and χ is the Taylor-Quinney coefficient, which represents the proportion of plastic work converted into heat. The Taylor-Quinney coefficient is an empirical constant and is often set to $\chi = 0.9$ in numerical simulations of adiabatic processes [22].

2.3.2 The Cockcroft-Latham Fracture Criterion

Cockcroft and Latham [23] did research on ductility and workability of metals in 1968 in order to propose a ductile fracture criterion. The criterion considers the effects of stress triaxiality, plastic strains and the Lode angle. The criterion is a particularly simple criterion as the fracture parameter W_c is the only model constant, hence the criterion is easy to calibrate from a single uniaxial tension test. The Cockcroft-Latham (CL) fracture criterion is given as

$$\omega = \frac{1}{W_c} \int_0^p \langle \sigma_I \rangle dp = \frac{1}{W_c} \int_0^p \langle \sigma^* + \frac{2}{3} \cos \theta_L \rangle \sigma_{eq} dp \quad (2.21)$$

where ω is the damage variable. Fracture is assumed to occur when $\omega = 1$. The σ_I is the maximum principal stress and $\langle \sigma_I \rangle = \max(\sigma_I, 0)$, which indicates that damage cannot occur when there is no tensile stress operating. The stress triaxiality is defined as $\sigma^* = \sigma_H / \sigma_{eq}$, where σ_H is the hydrostatic stress and the σ_{eq} is the von Mises equivalent stress. Further, θ_L is the Lode angle defined as

$$\cos(3\theta_L) = \frac{J_3}{2\sqrt{(J_2/3)^3}} \quad (2.22)$$

where $J_2 = \frac{1}{2} \sigma'_{ij} \sigma'_{ij}$ and $J_3 = \det \boldsymbol{\sigma}'$ are the second and third invariants of σ'_{ij} , respectively.

2.3.3 The Johnson-Cook Fracture Criterion

Johnson and Cook [24] presented in 1985 a fracture model which intended to show the relative effects of various parameters such as strain rate, temperature and pressure. The damage variable is given as

$$\omega = \int_0^p \frac{1}{p_f} dp \quad (2.23)$$

where the fracture strain p_f is defined as

$$p_f = \left[D_1 + D_2 \exp(D_3 \sigma^*) \right] (1 + \dot{p}^*)^{D_4} (1 + D_5 T^*) \quad (2.24)$$

where D_1, D_2, D_3, D_4 and D_5 are material constants. Fracture is assumed to occur when $\omega = 1$.

In a uniaxial tension test, when the specimen starts to neck, the stress state changes from purely uniaxial to a triaxial stress state. An expression for the initial stress triaxiality is given as

$$\sigma^* = \frac{1}{3} + \ln \left(1 + \frac{a}{2R} \right) \quad (2.25)$$

where R is the notch radius and a is the radius of the specimen in the notch.

2.4 Experimental Measurement Techniques

Deformation of a specimen can be measured in several ways, depending on the size of the specimen, environmental conditions, and measurement requirements for accuracy and precision of expected strain levels. In this thesis, four different measurement techniques are used, namely edge tracing, laser micrometer, DIC and extensometer. The different techniques are briefly described here.

2.4.1 Edge Tracing

Kristensen et al. [17] wrote a technical report on edge tracing in tensile tests using optical measurements. A short description of the method is presented here.

Edge tracing is a non-contact measurement technique which measures the smallest diameter of an axisymmetric specimen, and hence makes it possible to calculate the true stress-strain curve up to a deformation beyond diffuse necking. Edge tracing of tension tests have previously been conducted by directing a laser at the point of the cross-section with the smallest diameter by manual adjustments. Although laser measurements for edge tracing is an accurate method at ambient temperatures, the laser cannot be used for testing at temperatures below approximately 0°C or above approximately 70°C. This method has therefore been optimized using an optical measurement technique. This new method simplifies this procedure and can be conducted at high and low temperatures.

The optical measurements for edge tracing are conducted with the software eCorr [17]. In the laboratory, the diameter reduction measures from two angles using two cameras, or one camera in combination with two mirrors. The result is a picture series of the whole edge along the gauge length of the specimen. The software processes the recordings and can easily find the position of the smallest cross-section.

2.4.2 Laser Micrometer

Lasers are non-contact sensors that can be used in several different ways of measure the dimensions and positions of specimens. The sensing of outside diameters of cylindrical specimens is probably the most common application of a laser scanner gauge. The ASM handbook [25] describes how the laser operates as following.

A scanning laser beam gauge consists of a transmitter, a receiver and electronics to process the optical signal. A thin band of scanning laser light is projected from the transmitter to the receiver. When an object is placed in a beam, it casts a time-dependent shadow. Signals from the light entering the receiver are used by the microprocessor to extract the dimension represented by the time difference between the shadow edges. The gauges can exhibit accuracies as high as $\pm 0.25 \mu\text{m}$ for diameters of 10 to 50 mm.

In this thesis, a dual axis laser micrometer is used in the experimental work. A dual axis laser micrometer projects two perpendicular light beams towards a detector located on the opposite side of the specimen. The two orthogonal lasers create a box of laser light around the minimum cross-section of the specimen and measure the change in diameter [26]. The dual axis laser micrometer has a repeatability up to $\pm 0.01 \mu\text{m}$ [27].

2.4.3 Digital Image Correlation

Digital Image Correlation (DIC) is a non-contact optical method for measuring displacement fields. Based on the measured displacement fields, the strain fields may be obtained. This technique is simple to use and cost effective as well as more accurate compared to traditional techniques such as extensometers and strain gauges. DIC has therefore a huge range of applications.

The two-dimensional DIC method using a single fixed camera is limited to in-plane deformation measurements of the planar object surface. For curved surfaces, or three-dimensional deformation, a direct 3D extension of the 2D DIC must be applied as the 2D DIC method is no longer applicable. In this thesis, a 2D version of the DIC method is utilized.

The DIC technique involves finding the deformation of a surface by comparing digital images of the undeformed and deformed configuration. The DIC method comprises of three consecutive steps [28]. First, specimen and experimental preparations which includes applying a random speckle pattern on the surface of the specimen. This pattern carries the surface deformation information. Second, a camera records images of planar specimen surface before and after loading. And third, processing of the acquired images using a computer program to obtain the desired displacement and strain information. In this thesis, the in-house software eCorr [17] is used to process the recorded image series from the tests. The reader is referred to e.g. Fagerholt [16] for description of the DIC algorithm in details.

The DIC method has both advantages and disadvantages. The main advantages are simple experimental set-up and specimen preparation, low requirements in measurement environment (suitable for both laboratory and field applications) and wide range of sensitivity and resolution. The disadvantages are that the surface of the specimen must have a random speckle pattern and the measurements depend heavily on the quality of the imaging system.

2.4.4 Extensometer

An extensometer measures the elongation of a specimen during load application. Extensometers are widely used in tension tests and can provide a high degree of accuracy. There are mainly two types of extensometers: contact and non-contact.

A clip-on extensometer is a contact-type extensometer which is mounted directly on the specimen. There is practically no relative movement between the specimen and the extensometer, resulting in a high level of measurement accuracy. Typical extensometers have fixed gauge lengths and are classified by maximum percentage elongation. In this thesis, a clip-on extensometer is used in the experimental work.

Examples of non-contact extensometers are laser extensometer and video extensometer. The reader is referred to e.g. House and Gillis [6] for more details regarding extensometers.

2.5 Nanostructure Model

In structural designs, mechanical testing is part of the process of evaluating new materials, but it is both time consuming and expensive. A method for analysing the structural response without experimental testing would save both time and money. One such method is the nanostructure model.

The nanostructure model (NaMo) is a software developed by Ole Runar Myhr and

co-workers at Hydro, which determines the stress-strain curves of materials based solely on the chemical composition and the thermal history of the alloy. NaMo consists of three sub models; a precipitation model, a yield strength model and a work hardening model. Figure 2.3 illustrates the three sub models of the NaMo and how they interact.

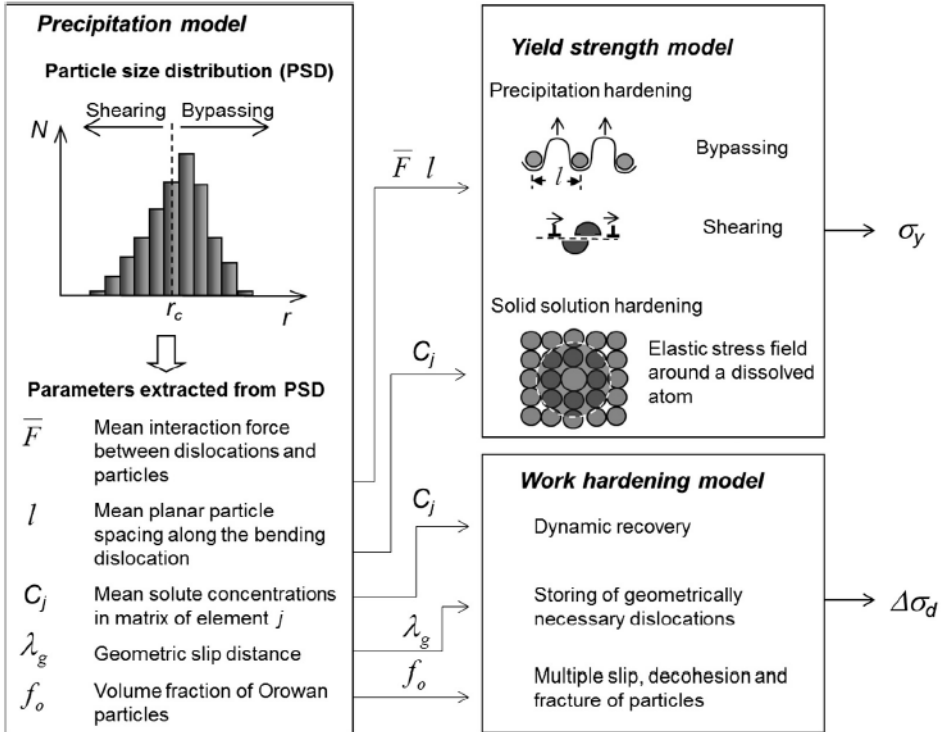


Figure 2.3: Illustration of the three sub models in NaMo. Adapted from Johnsen et al. [29].

The results from the precipitation model are the key components in the yield strength and work hardening models. The precipitation model calculates the evolution of the particle size distribution with time and temperature. The yield strength model converts the relevant output parameters from the precipitation model into equivalent room temperature yield stress, while the work hardening model takes the results from the precipitation model and uses it to calculate the work hardening at room temperature. The stress-strain curves predicted by NaMo can be then used in finite element simulations [29].

In 2015, the nanostructure model was extended to account for cold deformation and prolonged room temperature storage prior to artificial ageing. This extended model is called Namo-Version 2. Further details on Namo-Version 2 are given in Myhr et al. [30].

NaMo is verified and validated for 6XXX series aluminium alloys only. Since a 3XXX series aluminium alloy is investigated in this thesis, NaMo cannot be used here. It is however an interesting tool that can be used as an alternative method to determine the stress-strain curves of 6XXX series aluminium alloys instead of doing material testing.

3 | Experimental Work

The main objective behind the experimental work in this thesis has been to investigate how different measurement techniques and specimen geometries affect the calibration of constitutive relations and failure criteria for nonlinear finite element simulations of structural problems. In the following, quasi-static tension tests on four different specimen geometries have been carried out by using different measurement techniques. The different techniques are here described and the experimental results are presented and discussed.

3.1 Material Description

In this thesis an aluminium alloy of the 3XXX series with major alloying elements of manganese has been investigated. The material was provided as DC-cast extrusion ingots with a diameter of 100 mm produced at the laboratory casting facilities at Hydro Aluminium R&D Sunndal. The material was provided for Westermann et al. [26, 31] and Pedersen et al [32]. Aluminium alloys from the 3XXX series provide moderate strength and good corrosion resistance, in addition to low density and good formability. The 3XXX series alloys are also suited for use at elevated temperatures. In order to secure adequate mechanical strength for many engineering applications, aluminium alloys are very often heat treated. However, the alloys from the 3XXX series are non-heat treatable but the strength may be increased through work hardening. Today, the major applications of the 3XXX series aluminium alloys are heat exchangers in vehicles and power plants, while other applications are kitchen equipment as pots and pans. As the 3XXX series alloys have moderate strength, applications in structural designs are precluded. The exact chemical composition of the material is presented in Table 3.1. Throughout this thesis the aluminium alloy from the 3XXX series will be referred to as Al1.2Mn to ease the reading.

Table 3.1: Chemical composition of Al1.2Mn in weight % [26].

Fe	Mn	Mg	Si	Al
0.2	1.2	-	0.05	Bal.

During casting of Al1.2Mn, grain refiner (titanium boron (TiB)) has been added to control the grain size and avoid abnormal grain growth, which resulted in a homogeneous

grain structure. Otherwise the Al1.2Mn is as-cast without any further treatment after homogenisation [26].

3.2 Geometries

The specimen geometries in this thesis were small and large specimens with round cross-section and small and large flat specimens with dog-bone shaped cross-section. The geometries of the round specimens are shown in Figure 3.1. The round specimens have a parallel region in the middle of the specimen in which the gauge length is specified. The small and the large round specimens have gauge lengths of 5 mm and 40 mm, respectively. The round specimens were created with threaded ends.

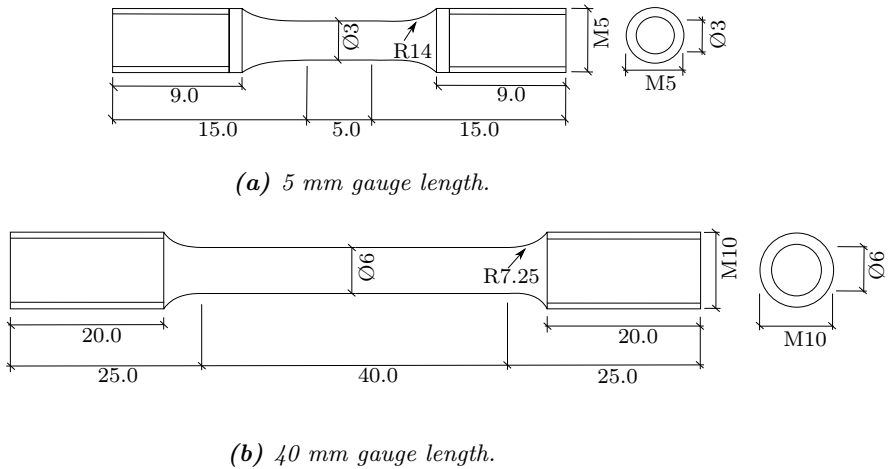


Figure 3.1: Geometries of the round specimens.

The geometries of the small and large flat specimens are shown in Figures 3.2 and 3.3, respectively. The flat specimens were created with circular holes at each end of the specimen in order to pin the specimens to the test machine. The gauge region consists of a parallel section in the middle of the specimen, where the small and large specimens have gauge lengths of 20 mm and 50 mm, respectively.

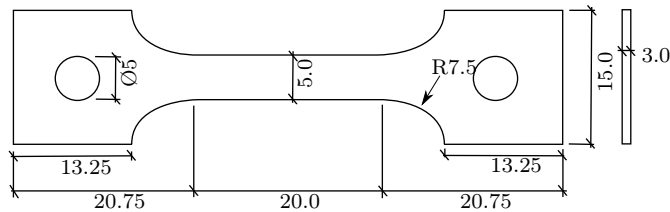


Figure 3.2: Geometry of the flat specimen with 20 mm gauge length.

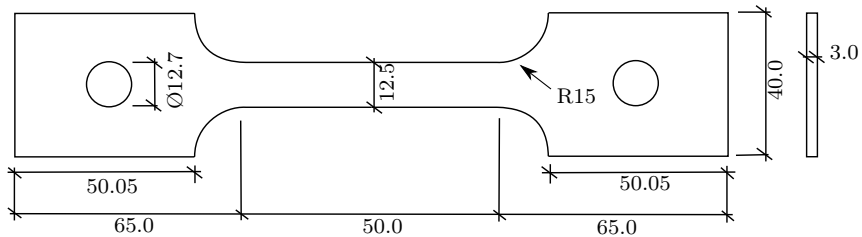


Figure 3.3: Geometry of the flat specimen with 50 mm gauge length.

3.3 Test Setup

Quasi-static tension tests are performed to provide information about material properties such as strength, ductility, hardening and toughness. Tension tests are usually performed in a hydraulic machine where the loading is either force or displacement controlled. The test setup is here described for each measurement technique.

3.3.1 Edge Tracing

The quasi-static tension tests of the round specimens were performed using an Instron 5982 test machine with a load cell of 5 kN. When performing a quasi-static tension test, the displacement rate of the test machine must be small enough in order to neglect the inertia forces in the system. A constant strain rate of $5 \times 10^{-4} \text{ s}^{-1}$ was therefore used in the tests. The initial diameter of the specimens, given in Appendix A.1, was measured prior to the tests.

The round specimens were installed in the test machine. The threaded ends were mounted into the machine, where the lower end was fixed and the loading was applied at the upper end. The velocity of the test machine was calculated as $v = \dot{\epsilon}L_0$, where $\dot{\epsilon}$ is the strain rate and L_0 is the gauge length of the specimen. The test machine was given a constant velocity of 0.15 mm/min for the specimens with 5 mm gauge length and 1.2 mm/min for the specimens with 40 mm gauge length, both corresponding to the given strain rate of $5 \times 10^{-4} \text{ s}^{-1}$ to assure quasi-static conditions.

The continuously change in cross-sectional diameter was captured by two Prosilica GC2450 cameras. The cameras have high resolution and a frame rate of 15 frames per second. The lens used was a Sigma 1:2.8 105 mm DG Macro lens. The test setup is shown in Figure 3.4a. The two cameras were placed with an angle of 90° , giving pictures in two perpendicular directions. The recorded pictures were to be processed in the in-house software eCorr, using edge tracing. In eCorr, the gray-scale gradient between the specimen and the background is used to detect the gauge region of the specimen. To optimize the gray-scale gradient, powerful lights of the type Hayashi HDF7010 were placed behind the specimen to overexpose the background and this resulted in a sharp contrast between the bright background and the dark specimen [17]. In addition to the recorded

pictures, the displacement of the cross-head and the applied force were measured. For the round specimens, four tests were successfully conducted for both geometries.

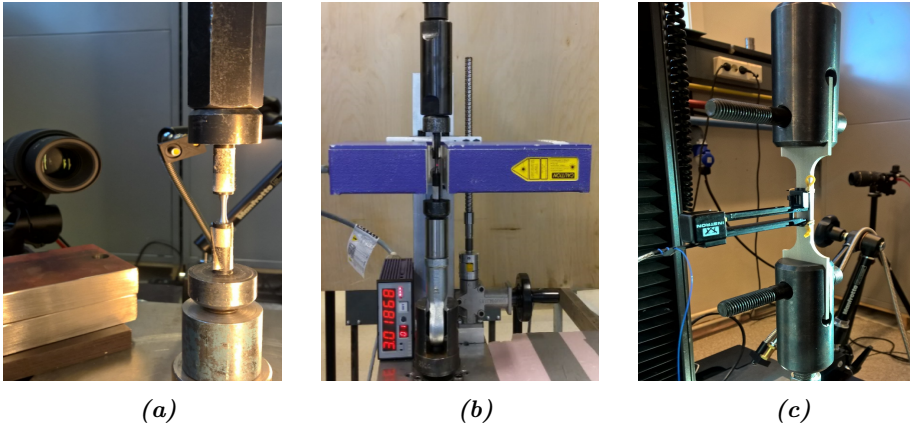


Figure 3.4: (a) Cameras and edge-trace approach, (b) Laser micrometer setup, (c) Extensometer.

3.3.2 Laser Micrometer

The quasi-static tension tests of the round specimens with 5 mm gauge length were in addition performed using an AEROEL XLS 13XY laser micrometer, which continuously measured the change in diameter of the specimens. In this case, a Zwick Roell Z030 - 30 kN test machine was used. The specimens were mounted in the test machine which was given a constant velocity of 0.15 mm/min, corresponding to a strain rate of $5 \times 10^{-4} \text{ s}^{-1}$. The laser, shown in Figure 3.4b, creates two perpendicular beams, each measuring $13 \times 0.1 \text{ mm}^2$, giving continuous measurements of the diameter in two perpendicular directions. The laser can be moved in the vertical direction, which is necessary in order to ensure that the minimum cross-sectional area was measured at all times. Three successful tests of the round specimens L5 were performed using laser.

3.3.3 DIC

The quasi-static tensions tests of the flat specimens were performed using the Instron 5982 test machine with a 5 kN load cell. The initial thickness and width of the specimens were measured prior to the tests in case of deviation from the nominal values. The initial values are given in Appendix A.1.

The flat specimens were pinned to the test machine through the two circular holes at each end of the specimen. As previously, the specimens were fixed at the lower end and the loading was applied at the upper end. The test machine was given a constant velocity of 0.6 mm/min for the flat specimens with 20 mm gauge length and 1.5 mm/mm for the

flat specimens with 50 mm gauge length. Both velocities correspond to a strain rate of $5 \times 10^{-4} \text{ s}^{-1}$ to assure quasi-static conditions.

Two-dimensional DIC was used to measure the elongation of the flat specimens. The 2D-DIC worked as an optical extensometer. The elongation of the specimens was captured by a camera perpendicular on the surface of the specimens, which resulted in a picture series that were to be processed in eCorr. To be able to extract the elongation in eCorr, a speckle pattern was spray-painted on to the gauge region of the specimens prior to the tests. By adding white paper as a background as well as powerful lights in the front, the contrast between the background and the specimen was optimized. For the flat specimens, four tests were successfully conducted for both geometries.

3.3.4 Extensometer

A clip-on extensometer was used at one of the tests of the flat specimens and the round specimens with 40 mm gauge length. The experimental setup with the extensometer is shown in Figure 3.4c. The extensometer has a gauge region of ± 5 mm, hence the extensometer was removed when its elongation reached 5 mm. The data from the extensometers can then be compared with the results from the edge-trace approach and the DIC approach.

3.4 Experimental Results

In this section the experimental results from the tension tests are presented. The procedure of extracting material data when using the different measurement techniques are described and the results from the tests of each specimen geometry are presented separately. In order to ease the reading, the round specimens with 5 mm and 40 mm gauge lengths are referred to as round specimen L5 and L40, respectively. In addition, the flat specimens with 20 mm and 50 mm gauge lengths are referred to as flat specimen L20 and L50, respectively.

3.4.1 Displacement of the Cross-Head

To evaluate the experimental results without considering the different measurement techniques, the total displacement of the cross-head was investigated. Figure 3.5 shows the force-displacement curves from the cross-head for the four specimen geometries. Note that for the round specimen L5 the data were supplied from the test machine (Zwick Roell Z030) using the laser setup, while the data for the three other geometries were from the same test machine (Instron 5982). In Figures 3.5a and 3.5c a slight scatter is observed, otherwise there is a good agreement within each geometry.

A representative test from each geometry was chosen and the engineering stress-strain curves from the cross-head are compared in Figure 3.6. To accurately compare the results, the Young's modulus needed to be corrected according to the nominal value. The measured and the nominal Young's modulus were corrected by adjusting the initial stiffness

of the stress-strain curves. This was done through the relation

$$\Delta\varepsilon = \varepsilon_c - \varepsilon_m \Rightarrow \varepsilon_c = \varepsilon_m + \Delta\varepsilon = \varepsilon_m + \left(\frac{E_m - E_c}{E_m E_c} \right) \sigma \quad (3.1)$$

where subscript c means corrected and m means measured. The correct Young's modulus equals the nominal Young's modulus for aluminium alloys, i.e., $E_c = E = 70000$ MPa. It is observed in Figure 3.6 that both the yield stress at 0.2 % strain and the strain level at diffuse necking varies for the different geometries. However, the stress level at diffuse necking coincides.

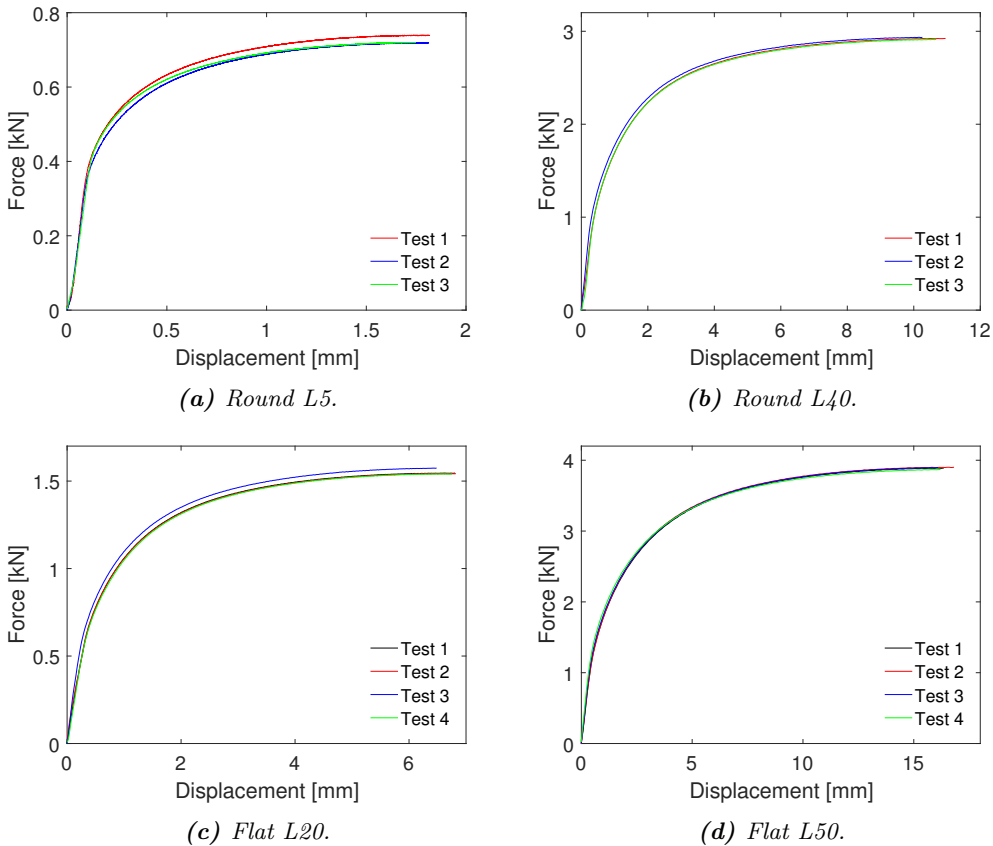


Figure 3.5: Force-displacement curves from the displacement of the cross-head.

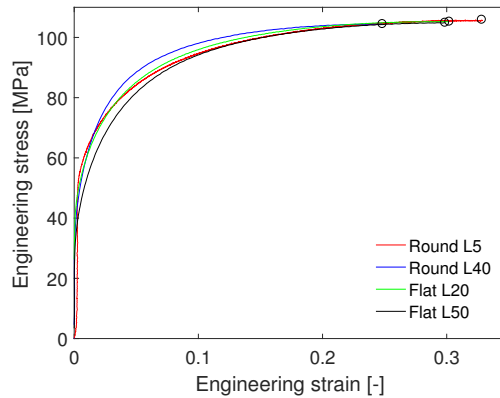


Figure 3.6: Engineering stress-strain curves from the displacement of the cross-head. The black o indicates diffuse necking.

3.4.2 Round Specimen L5

Edge Tracing

To extract material properties of a specimen when using cameras and edge tracing as the measurement technique, the experimental data have to be processed in the software eCorr. The output from the software was the minimum diameter in two perpendicular directions, denoted D_1 and D_2 . In addition, a log-file from each test containing measurements of time, force and displacement was available after testing. In eCorr, the recordings from the experiment were processed and the minimum diameter was measured. Figure 3.7 shows the gauge region of a round specimen with the minimum diameter (pink line) highlighted. The minimum diameter was found as the minimum vertical distance between the two edges of the specimen (blue lines).

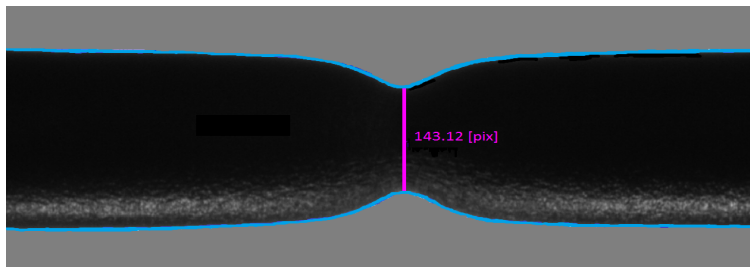


Figure 3.7: Determination of the minimum diameter in eCorr.

The output from eCorr with measurements of the minimum diameter D_1 and D_2 , given in number of pixels, was processed in MATLAB. As the minimum diameters were given in number of pixels, a mm/pixel relation needed to be established. In eCorr, the

vertical distance between the edges of the undeformed specimen was measured using an image ruler. The initial diameter of the specimen measured in the laboratory was then divided by the vertical distance from eCorr, giving a mm/pixel relation. The diameter reduction in each direction was then calculated using

$$\Delta D_1 = D_{1,0} - D_1, \quad \Delta D_2 = D_{2,0} - D_2 \quad (3.2)$$

where the $D_{1,0}$ and $D_{2,0}$ are the initial diameters in direction 1 and 2, respectively. As the current diameter was continuously measured in two directions, an indication of material isotropy could be evaluated by comparing the force-diameter reduction in direction 1 and 2. The cross-sectional area of the round specimens was assumed to be elliptical. The initial and current cross-sectional area of the specimen were calculated from

$$A_0 = \frac{\pi}{4} D_{1,0} D_{2,0}, \quad A = \frac{\pi}{4} D_1 D_2 \quad (3.3)$$

respectively. The current cross-sectional area of the specimen was continuously measured during the test, so the true (Cauchy) stress and the logarithmic strain were calculated directly by using Equations 2.3 and 2.4. The Young's modulus for aluminium alloys has a nominal value of $E = 70000$ MPa. The measured Young's modulus from a quasi-static tension test often differs from the nominal value, therefore the measured Young's modulus was corrected using Equation 3.1.

The true stress-logarithmic strain curves for the round specimens L5 are plotted in Figure 3.8a. To investigate repeatability, all four tests are plotted together. The observed stress level at failure coincides for all four tests, however there is a slight variation in strain level at failure. The different tests display a good repeatability. To evaluate the material isotropy, the force-diameter reduction curves in direction 1 and 2 for a representative test are compared in Figure 3.8b. As seen, the curves in direction 1 and 2 have a good agreement and the material behaves isotropic. Another indication of the material isotropy is the r-value. The r-value is the ratio of the strain increments measured at minimum cross-section,

$$r = \frac{d\varepsilon_1}{d\varepsilon_2}, \quad \varepsilon_1 = 2 \ln \left(\frac{D_1}{D_{1,0}} \right), \quad \varepsilon_2 = 2 \ln \left(\frac{D_2}{D_{2,0}} \right), \quad (3.4)$$

where an r-value equal to unity indicates isotropic behaviour. Figure 3.8c presents the r-value for a representative test of the round specimen L5. The r-value is approximately unity throughout the test, indicating isotropic material behaviour. The Al1.2Mn has been homogenised and assumed isotropic which corresponded well with the observations made from the experimental results.

The material data were found from the processed data. The stress and strain at diffuse necking, denoted with the subscript u , were found at the maximum force level, F_{max} , as described in section 2.2. The corresponding values at failure, denoted with the subscript f , were found at maximum true stress, $\sigma_{t,max}$. In addition, the yield stress at 0.2 % strain, $\sigma_{0.2}$, was found. The extracted material data are given in Table 3.2 in Section 3.4.3, together with the results from the tension tests of the round specimens L40. The

$\varepsilon_{l,f,micro}$ is the fracture strain of the specimen when the diameter is measured using an optical microscope. The area and the strain at fracture were calculated using

$$A_f = \frac{\pi}{4} D_{1,f} D_{2,f}, \quad \varepsilon_f = \ln \frac{A_0}{A_f} \quad (3.5)$$

respectively. $D_{1,f}$ and $D_{2,f}$ are the diameters at fracture in direction 1 and 2, respectively.

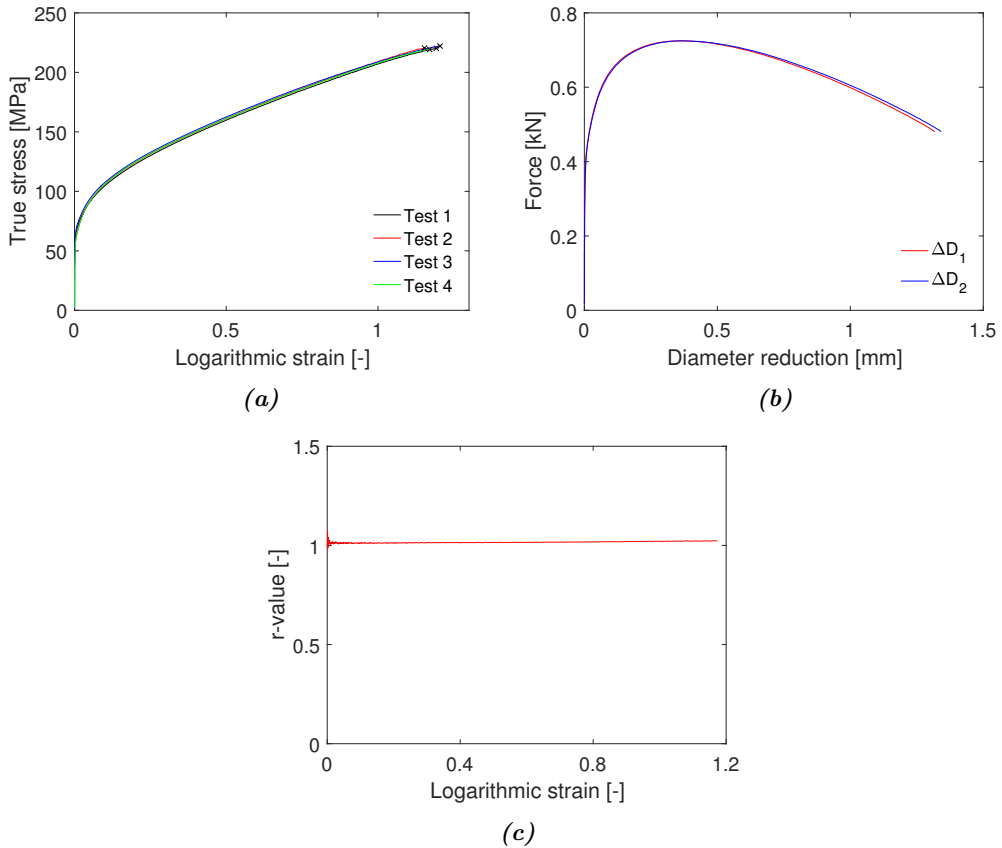


Figure 3.8: (a) True stress-logarithmic strain curves for the round specimens L5 using edge-trace. The black x marks the point of failure, (b) Force-diameter reduction curves in direction 1 and 2 for a representative test (test 4), (c) r -value-logarithmic strain for a representative test (test 4).

Laser Micrometer

The experimental results from the quasi-static tension tests using laser micrometer were supplied in a spreadsheet containing measurements of time, force, position, diameter D_1

and diameter D_2 . As the laser continuously measured the diameter of the specimens, the experimental data could be imported directly to MATLAB and further processed.

When using a laser micrometer to measure the current diameter, the search for the smallest diameter resulted in small jumps in the diameter measurements. To get a smooth curve the small jumps had to be removed. When the small jumps were removed, the further procedure of extracting the material data was the same as described for the edge-trace approach above. Figure 3.9a compares the true stress-logarithmic strain curves for the round specimens L5 using laser. As observed, the three tests display a good repeatability, however there is a slightly variation in strain level at failure. The force-diameter reduction curves in direction 1 and 2 for a representative test are displayed in Figure 3.9b and the r-value-logarithmic strain curve for a representative test is presented in Figure 3.9c. As observed, the laser measurements show a good agreement in the two directions and the r-value indicates isotropic behaviour.

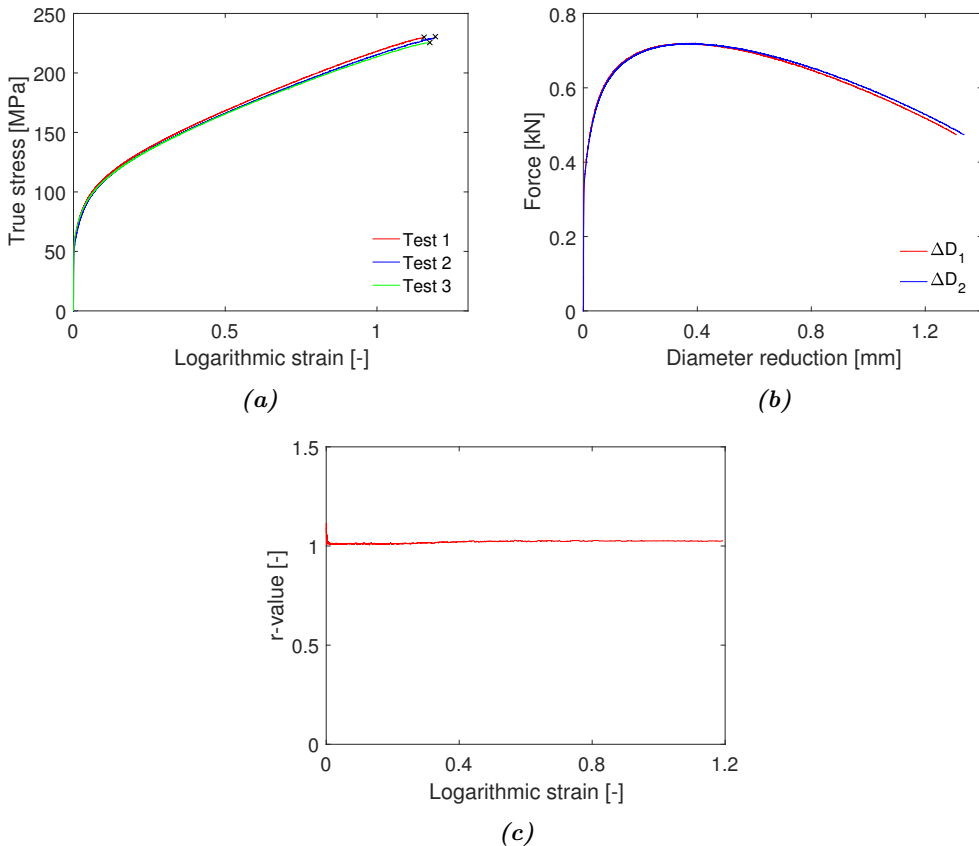


Figure 3.9: (a) True stress-logarithmic strain curves for the round specimens L5 using laser. The black x marks the point of failure, (b) Force-diameter reduction curves in direction 1 and 2 for a representative test (test 2), (c) r-value-logarithmic strain for a representative test (test 2).

The material data obtained from the laser measurements are given in Table 3.2 in Section 3.4.3. The deformed geometry of a representative test of the round specimen L5 are shown in Figure 3.10. The fracture surface will be examined in Section 3.5.

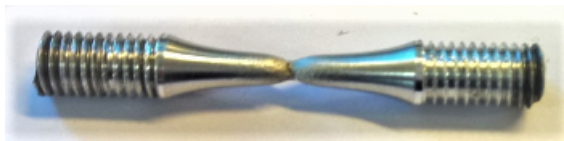


Figure 3.10: Deformed geometry of a representative test from the round specimen L5.

3.4.3 Round Specimen L40

Edge Tracing

The procedure of extracting material data of a tensile specimen when using edge tracing as the measurement technique was described in Section 3.4.2. The true stress-logarithmic strain curves for the round specimens L40 are plotted in Figure 3.12a. As seen, Test 2 has a slightly higher stress and strain level at failure, otherwise the tests coincide. Figure 3.12b shows the force-diameter reduction curves in direction 1 and 2 and Figure 3.12c presents the r-value-logarithmic strain curve for a representative test. As observed, the r-value is approximately unity, which indicates that the round specimen L40 behaves isotropic. The extracted material data for the round specimen L40 are given in Table 3.2.

Extensometer

Test 4 of the round specimen L40 was performed using an extensometer in addition to the cameras and edge-trace approach. As the extensometer was placed in the gauge region of the specimen, the recorded images were disturbed and thus the data from test 4 could not be processed in eCorr. However, the engineering stress-strain curve from the extensometer was extracted and compared with a representative test. Figure 3.12d shows the engineering stress-strain curves up to diffuse necking. As seen, the stress level of the two curves coincide, hence the extensometer and the edge-trace approach give similar results. The extensometer was removed when an elongation of 5 mm was reached, which was before diffuse necking of the specimen in this case.

The deformed geometry of a representative test from the round specimen L40 are shown in Figure 3.11.

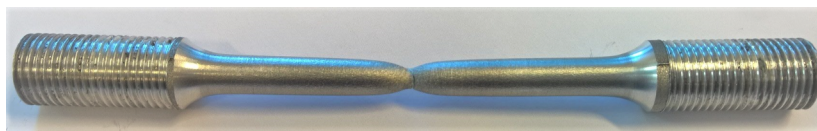


Figure 3.11: Deformed geometry of a representative test from the round specimen L40.

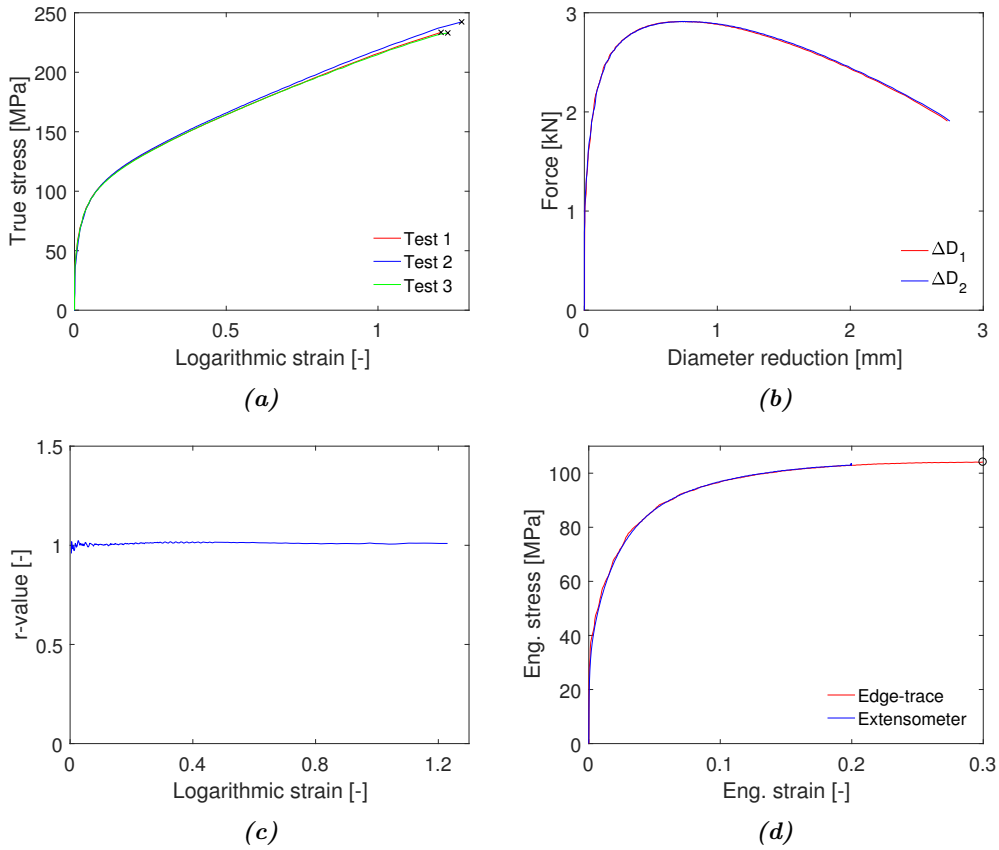


Figure 3.12: (a) True stress-logarithmic strain curves for the round specimens L40 using edge tracing. The black x marks the point of failure, (b) Force-diameter reduction curves in direction 1 and 2 for a representative test (test 3), (c) r-value-logarithmic strain for a representative test (test 3), (d) Engineering stress-strain curves from the extensometer (Test 4) and edge-trace (Test 3). The black o indicates diffuse necking.

Table 3.2: Material data from the tension tests of the round specimens.

Geometry	Method	Test No.	$\sigma_{0.2}$ [MPa]	$\sigma_{e,u}$ [MPa]	$\varepsilon_{e,u}$ [-]	$\sigma_{t,u}$ [MPa]	$\varepsilon_{t,u}$ [-]	$\sigma_{t,f}$ [MPa]	$\varepsilon_{l,f}$ [-]	$\varepsilon_{l,f,micro}$ [-]
Round L5	Edge-trace	Test 1	61.85	101.3	0.3073	132.6	0.2679	220.2	1.193	1.437
		Test 2	55.61	102.4	0.3144	134.6	0.2734	220.5	1.155	1.400
		Test 3	61.57	103.2	0.2859	133.0	0.2515	222.1	1.205	1.442
		Test 4	51.40	102.6	0.3002	133.1	0.2625	219.2	1.174	1.510
	Laser	Test 1	56.67	107.3	0.3115	140.6	0.2712	230.0	1.155	1.329
		Test 2	52.65	105.9	0.3261	140.4	0.2822	230.5	1.194	1.382
		Test 3	57.80	105.4	0.3014	137.2	0.2635	225.6	1.175	1.302
		Test 4	40.77	104.5	0.2957	135.2	0.2590	233.5	1.208	1.346
Round L40	Edge-trace	Test 2	36.90	105.2	0.2926	135.8	0.2566	242.3	1.276	1.428
		Test 3	40.10	104.1	0.2998	135.3	0.2622	233.1	1.230	1.318

3.4.4 Flat Specimen L20

DIC

The procedure of processing the measured data from the tension tests of the flat specimens using DIC as the measurement technique are described here. A log-file from each test containing measurements of time, force and displacement was available after testing. In addition, the recorded pictures from the experiments were to be processed in eCorr in order to extract the material data.

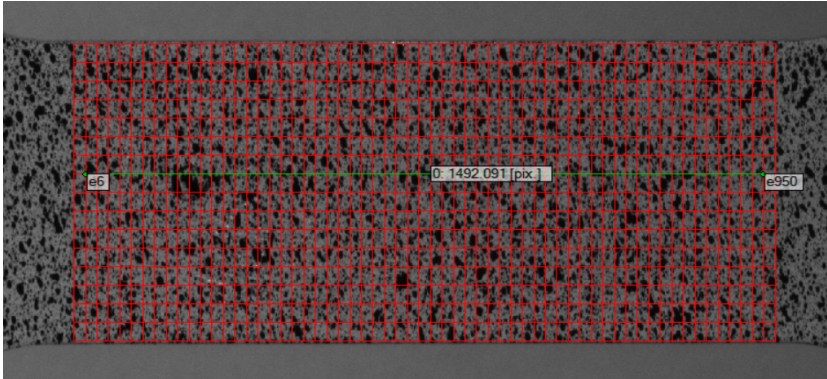


Figure 3.13: Illustration of the mesh of the gauge region of the undeformed specimen, with a vector (green line) which extracts the elongation of the specimen. The figure is taken from eCorr.

In eCorr, a mesh was created over the gauge region of the specimen consisting of structured, linear Q4 elements, as shown in Figure 3.13. The element size of 25 x 25 pixels was chosen to be ideal to the speckle pattern to extract the elongation as accurate as possible and to avoid noise. A vector was then created over the gauge region of the specimen in which the elongation was extracted. The data were further processed using MATLAB.

When the elongation of the specimen was extracted, the engineering stress and strain were calculated using Equation 2.1. Further, by using the relations in Equations 2.2 and 2.5, the true stress and the logarithmic strain until diffuse necking were calculated. In order to calculate the stresses and strains after diffuse necking, the current area of the specimen had to be measured. As the deformation in the thickness direction cannot be measured directly with the 2D-DIC, only the data until necking are evaluated in this section. The true stress-logarithmic strain curves for the flat specimens L20 are plotted in Figure 3.14a. As observed, Test 3 has a lower strain level at diffuse necking. Otherwise there is a good agreement within the tests. The force-displacement curve for a representative test is displayed in Figure 3.14b.

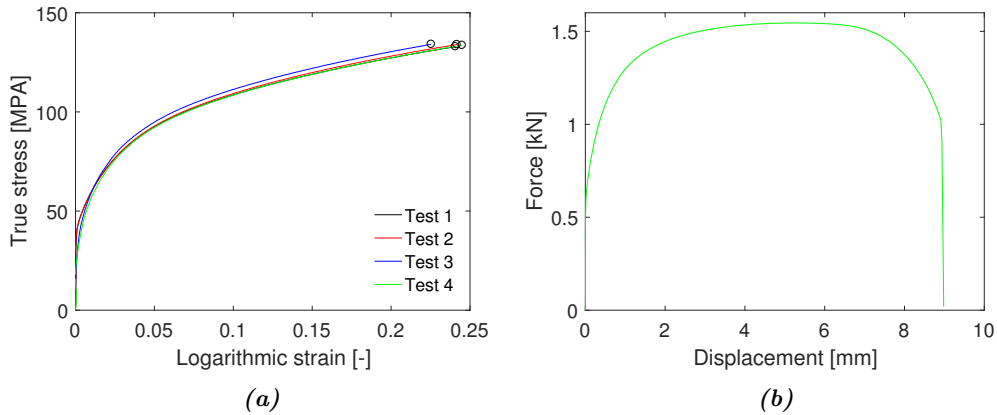


Figure 3.14: (a) True stress-logarithmic strain curves for the flat specimens L20 using DIC. The black o indicates diffuse necking. (b) Force-displacement curve for a representative test (test 1) all the way to fracture.

Extensometer

For the flat specimens L20 a clip-on extensometer was used in one of the tests. In Figure 3.15 the engineering stress-strain curves until diffuse necking for the extensometer and a representative test using DIC are compared. The curves coincide, hence the extensometer and the DIC approach give similar results. It is also observed that the point of necking coincides. The extensometer was removed when its elongation had reached 5 mm, which corresponded to diffuse necking in this case. This indicates that the elongation of the specimen at diffuse necking was approximately 5 mm.

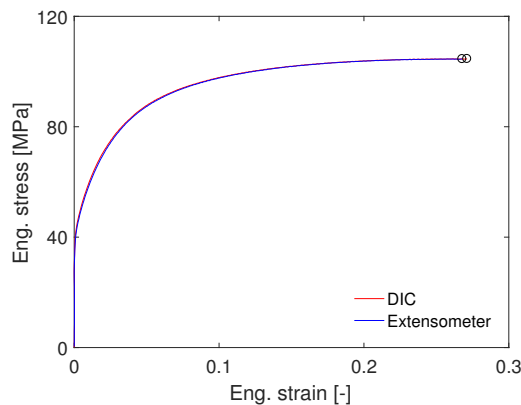


Figure 3.15: Engineering stress-strain curves using extensometer and DIC. The black o indicates diffuse necking.

The deformed geometry of a representative test of the flat specimen L20 is shown in Figure 3.16. The fracture surface will be examined in Section 3.5. The material data found from the processed data of flat specimen L20 are displayed in Table 3.3 in Section 3.4.5.



Figure 3.16: Deformed geometry of a representative test from the flat specimen L20. The speckle pattern spray-painted on to the gauge region prior to the test is visible.

3.4.5 Flat Specimen L50

DIC

The procedure of processing the experimental results from the tension tests of the flat specimens L50 when using DIC as the measurement technique was described in section 3.4.4. As for the flat specimens L20, only the data until diffuse necking are evaluated in this section. The true stress-logarithmic strain curves for the flat specimens L50 are compared in Figure 3.17a. Test 2 has slightly higher stress and strain level at diffuse necking, otherwise there is a good repeatability within the tests. Figure 3.17b shows the force-displacement curve for a representative test.

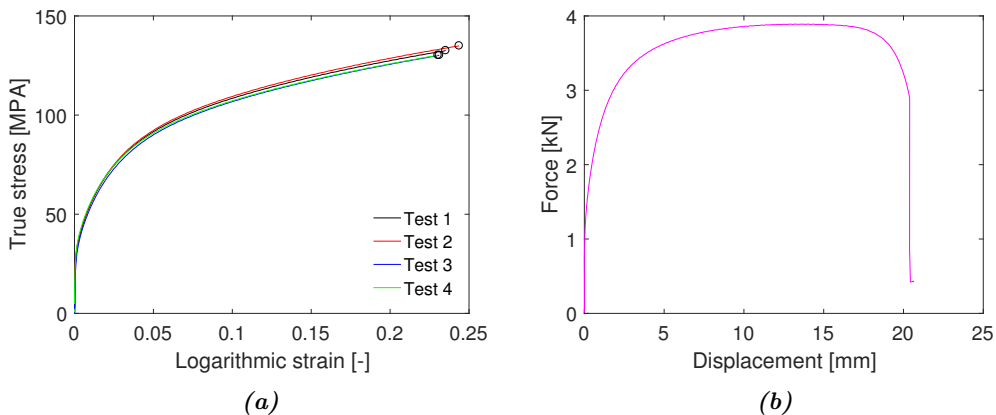


Figure 3.17: (a) True stress-logarithmic strain curves for the flat specimens L50 using DIC. The black o indicates diffuse necking, (b) Force-displacement curve for a representative test (test 1) all the way to fracture.

Extensometer

A clip-on extensometer of length 25 mm was used in one of the tests of the flat specimen L50. Figure 3.18 compares the engineering stress-strain curves from the extensometer and the DIC approach. The curves coincide, hence the extensometer and the DIC approach give similar results. As seen, the data from the extensometer were not measured all the way to diffuse necking. This is because the extensometer was removed when an elongation of 5 mm was reached, which was before diffuse necking of the specimen in this case.

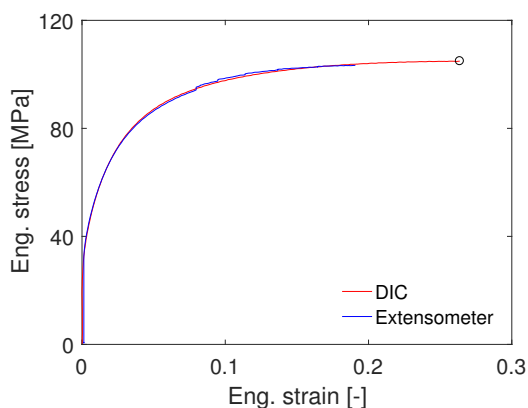


Figure 3.18: Engineering stress-strain curves using extensometer and DIC. The black o indicates diffuse necking.

The deformed geometry of a representative test from the flat specimen L50 is shown in Figure 3.19. The material data found from the processed data are given in Table 3.3.



Figure 3.19: Deformed geometry of a representative test of the flat specimen L50. The speckle pattern spray-painted on to the gauge region prior to the test is visible.

Table 3.3: Material data obtained from the tension tests of the flat specimens using DIC.

Geometry	Test No.	$\sigma_{0.2}$ [MPa]	$\sigma_{e,u}$ [MPa]	$\varepsilon_{e,u}$ [-]	$\sigma_{t,u}$ [MPa]	$\varepsilon_{t,u}$ [-]
Flat L20	Test 1	46.65	104.6	0.2712	133.0	0.2412
	Test 2	45.84	105.3	0.2732	134.0	0.2422
	Test 3	32.78	106.7	0.2573	134.2	0.2290
	Test 4	35.09	104.6	0.2785	133.7	0.2448
Flat L50	Test 1	36.58	104.9	0.2637	132.6	0.2352
	Test 2	37.62	105.9	0.2745	135.0	0.2437
	Test 3	34.70	103.5	0.2580	130.2	0.2312
	Test 4	38.37	103.3	0.2604	130.2	0.2303

3.5 Scanning Electron Microscope

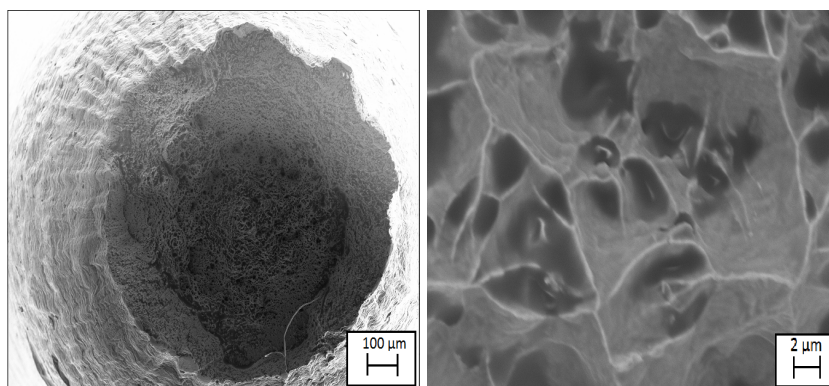
To get a better understanding of the fracture mechanisms of the material, the fracture surfaces of the round specimen L5 and the flat specimen L20 were studied using a Scanning Electron Microscope (SEM). A brief description of the SEM is given below, however the details are not included.

The Scanning Electron Microscope is a type of electron microscope which uses a focused beam of electrons to scan the surface of the specimen. The electrons interact with the atoms in the specimen which creates various signals that contain information about the topography, chemical composition and the crystalline structure of the material. These signals are captured by a detector, which produces an image. Here, only the topography of the fracture surface was studied. The SEM has some great advantages in comparison to an optical microscope. An optical microscope is limited by the wavelength of the illuminating light, while SEM is limited by the wavelength of the electrons. Since the wavelength of the electrons is about 10^{-5} of the wavelength of light, the SEM has many times better resolution than the optical microscope [33]. The combination of high spatial resolution and high depth of field makes the SEM one of the most versatile forms of microscope available, and an ideal tool to examine the microstructure of materials [34].

In the laboratory, the specimens were cleaned with acetone in order to remove dirt and grease. The specimen was mounted on a specimen stand with the fracture surface facing upwards and then placed inside the vacuum chamber. The vacuum prevents interaction between the electrons and air molecules on the way down to the specimen, which would produce noise in the image. The SEM machine used was a Zeiss Gemini SUPRA 55VP and the vacuum in the machine was $< 10^{-5}$ Pa. When the chamber reached the required level of vacuum, the electron gun was turned on and images of the specimen were created. The fracture surfaces could then be examined.

Figures 3.20 and 3.21 show the fracture surfaces of the round specimen L5 and the flat specimen L20, respectively. As seen in Figure 3.20a, the cleaning of the fracture surface did not remove all the dirt and a single hair is clearly visible in the lower right corner. The overview picture of the round specimen L5 shows the formation of the cup-and-cone fracture surface that is commonly observed in uniaxial tension tests for ductile

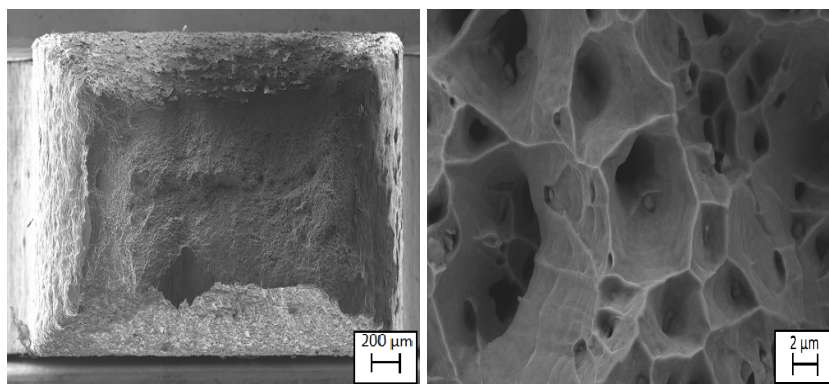
materials. The outer ring of the specimen, a region between the edges and approximately $100 - 200 \mu\text{m}$ towards the centre, contains relatively few voids, because the hydrostatic stress is lower than in the centre. The cup-and-cone fracture surface implies that the fracture starts from the centre and grows outward. As observed, the specimen exhibits a dimpled appearance, which is typically for microvoid coalescence. In Figures 3.20b and 3.21b the dimples structures are clearly visible and particles are observed at the bottom of some of the dimples. The clearly dimple structure observed for both geometries indicates ductile fracture.



(a) Overview.

(b) Zoom.

Figure 3.20: Round specimen L5.



(a) Overview.

(b) Zoom.

Figure 3.21: Flat specimen L20.

3.6 Discussion

In this thesis, quasi-static tension tests have been performed on specimens with four different specimen geometries, where different methods of extracting material data have been investigated. The experimental results from the different methods are here compared and discussed in order to investigate the similarities and differences of the methods, and compare their accuracy.

Displacement of the Cross-Head

A starting point in the discussion of the experimental results is to compare the engineering stress-strain curves extracted directly from the displacement of the cross-head, as the test machines were unaffected by the different measurement methods. Figure 3.6 shows the engineering stress-strain curves of representative tests from each specimen geometry. It is observed that the specimens display the same material behaviour to a certain degree. However, there is a difference in yield stress at 0.2 % strain and the smooth specimen L40 has a clearly lower strain level at diffuse necking and lower work hardening. Otherwise, the stress levels for the different geometries coincide at diffuse necking.

There are some uncertainties in extracting the material data directly from the displacement of the cross-head. The gripping of the specimens was different. The round specimens were threaded to the test machine, while the flat specimens were pinned. It was important to make sure that the specimens could be held at a maximum load without failure or slippage of the grip section. In this case, the pin could give some looseness or mobility of the specimen the moment the load was applied. Other factors that could influence the results were the accuracy and resolution of the load cell output or the alignment of the specimens in the test machines as two different test machines were used in the experimental work.

Laser vs. Edge Tracing

Figure 3.22 compares the true stress-logarithmic strain curves for a representative test of the round specimen L5 using laser and edge-trace and of the round specimen L40 using edge-trace. As seen, the round specimen L5 using laser and the round specimen L40 using edge-trace exhibit a good agreement until failure. The edge-trace measurements of the round specimens L5 shows clearly a lower stress level at failure, in addition to lower work hardening. The deviation in stress level between the round specimen L5 using laser and edge-trace was 11.3 MPa at failure, which corresponded to 4.89 %. This deviation is non-negligible and the sources of error are discussed below.

In quasi-static tension tests, the use of lasers is a well-known measurement technique and the accuracy is at a micrometer scale. In this thesis, the laser measurements are assumed correct and used as reference measurements. The sources of error due to the deviation in Figure 3.22 are therefore focused on the edge-trace approach.

The deviation in Figure 3.22 can be caused by several reasons. First, when processing the pictures in eCorr, the resolution of the pictures was not optimal. As seen in the Figure

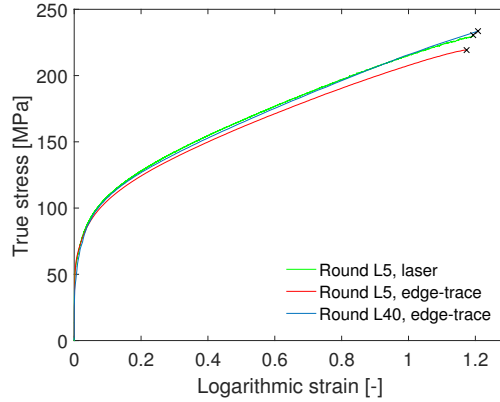


Figure 3.22: Comparison of true stress-logarithmic strain curves from the round tension tests.

3.7, the ratio between the horizontal and the vertical directions of the picture is not equal to one and the highest resolution will then be in the horizontal direction. Since the minimum diameter was measured in the vertical direction, a lower resolution gave blurry edges of the specimen and this could result in a ± 1 pixel deviation in the minimum diameter [35]. By reducing the minimum diameter with one pixel, the deviation was reduced only with 0.63 %. The resolution of the pictures was therefore not the decisive reason for the deviation in Figure 3.22, but it is important to keep this in mind.

A second source of error could arise during the experiment work. In the beginning of the test, when the force was applied and started to increase, the specimen could adjust its position and move towards or away from the cameras. This adjustment could influence the mm/pixel relation and result in an overall larger or smaller minimum diameter.

The third source of error could be the initial measurements of the specimens. Prior to the tests, the initial diameter, denoted D_0^{et} , was measured manually with a digital slide gauge. The digital slide gauge has an accuracy of 1/100 mm [36], which is a lower accuracy than the laser. When an inexperienced user utilized the glide gauge, small variations gave different measurements and this could affect the calculated stress levels. For the representative test of the round specimens L5 measurement of the initial diameter was forgotten in the laboratory, so the nominal diameter of 3 mm was used in the calculations. The initial diameters measured in situ with the laser, denoted D_0^l , varied between 2.943 - 2.964 mm, which indicated that the diameters were initially smaller than the nominal value. Figure 3.23 shows that a small reduction in initial diameter gives noticeable change in the stress level at failure. The values in the parentheses are the percentage error in stress level at failure between the laser and edge-trace approach.

As seen, when $D_0^{et} = D_0^l$ the true stress-logarithmic strain curves coincide for two methods and the error becomes relatively small. This indicates that D_0^{et} had a value close to D_0^l and using the nominal value gave a deviation, which demonstrates the importance of measuring the initial diameters of the specimens prior to the tests. When using the edge-trace approach, there is no standard guideline in how to measure the initial diameter

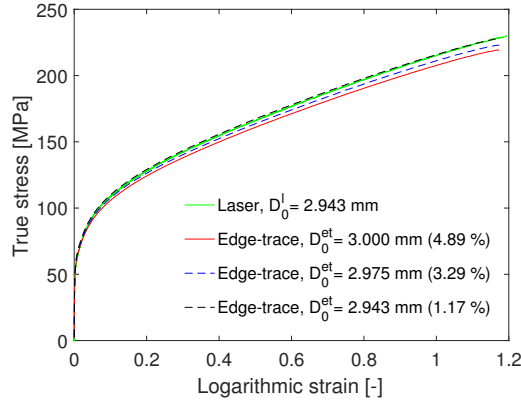


Figure 3.23: Initial diameters of the round specimen L5.

and the method varies from user to user, which affects the results.

Edge Tracing vs. DIC

Figure 3.24 compares the true stress-logarithmic strain curves until diffuse necking for the round specimens using edge-trace and the flat specimens using DIC. As seen, the round specimen L5 clearly shows a higher yield stress at 0.2 % strain and has a different behaviour. Note that the strain interval in Figure 3.24 is small compared to the strain interval in Figure 3.22 and the difference in yield stress is not as clear at larger strains (see Figure 3.22).

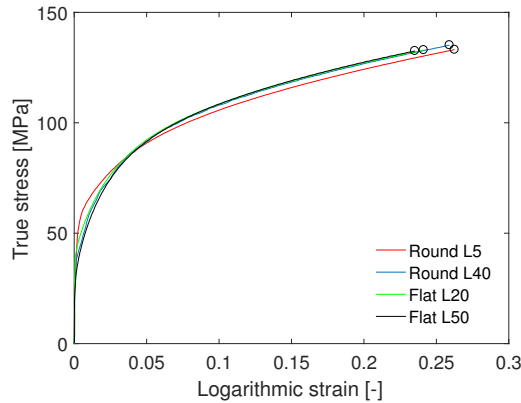


Figure 3.24: Comparison of the true stress-logarithmic strain curves until diffuse necking for the round and flat specimens.

It is observed in Figure 3.24 that the true stress-logarithmic strain curves for the round

specimen L40 and the flat specimens L20 and L50 exhibit similar behaviour. The stress level at diffuse necking coincide to a certain degree, but there is a slight variation in strain level at diffuse necking.

The measured data from the flat tension tests have only been evaluated until diffuse necking, hence the strain interval is small compared with the measured data from the round tension tests. To be able to compare the edge-trace and DIC approaches properly, the true stress-logarithmic strain curves calculated for the flat specimens need to be extrapolated. This will be done in Chapter 4. The method of extrapolating is an approximation which can lead to errors. When using the 2D-DIC method as an optical extensometer the extracted data were only valid until diffuse necking without combining it with FEM, hence the method has a major weakness compared with the edge-trace approach. This means that in order to accurately investigate fracture, the laser or the edge-trace approach have to be applied.

As discussed above, the measurements of the initial dimensions of the specimens prior to the tests were important for the results. The digital slide gauge was used to measure the initial dimensions of the flat specimens and using the same instrument consistently in each test gave an agreement in the result within the geometries, which was observed in Figures 3.14a and 3.17a.

When performing material tests on relatively small specimens the number of grains over the loading area of the specimens can have an influence on the results. Westermann et al. [26] studied in 2014 the effects of particles and solutes on ductile fracture of aluminium alloys, whereas one of the alloys was the Al1.2Mn used in this thesis. The reader is referred to Westermann et al. [26] for details on this study. All four specimen geometries in this thesis consist of Al1.2Mn but they have different geometries, which results in different areas. The Al1.2Mn consists of an equiaxed grain structure with a grain size of approximately $60\ \mu\text{m}$. As the grain size was approximately constant, the number of grains in each geometry varied. The round specimen L5 had an initial area of $7.07\ \text{mm}^2$, whereas the initial area of the flat specimen L20 was $15\ \text{mm}^2$. This meant that the flat specimen L20 had approximately twice as many grains over the cross-sectional area as the round specimen L5. As the force is carried by the grain structure in the specimens the number of grains over the loading area may results in different load capacity and hence different response.

In Figure 3.24 it is observed that the round specimen L5 has a clearly higher stress at yielding than the other specimen geometries. To investigate the reason for this deviation, new tension tests of the round specimen L5 using laser and edge-trace were performed in the laboratory. This time the initial diameters of the specimens were measured prior to testing to avoid errors regarding the initial measurements as discussed above. The results from the new tests showed the same deviation in yield stress as seen in Figure 3.24. This indicated that the initial measurements of the specimens were not the reason for the deviation in yield stress for the round specimen L5 and the reason for the deviation is unknown. One explanation could be that this was a scalar effect as the round specimen L5 had clearly smaller cross-sectional area than the other specimen geometries.

4 | Material Models

4.1 Calibration of Material Model

In the numerical simulations in Chapter 5, two calibration methods were used. Direct calibration of the measured data obtained from the tension tests and inverse modelling using the code LS-OPT [37]. In this chapter, the calibration of the material model based on the direct calibration is described.

The MJC constitutive relation with Power and Voce hardening laws were used in the calibration of the material model in order to examine their behaviour compared with the true stress-logarithmic strain curves from the experimental results.

4.1.1 Round Specimens

The calibration of the material constants in the MJC constitutive relation was performed using the measured data from the tension tests of the round specimens, where edge tracing was used as measurement technique. The representative tests chosen were Test 4 of the round specimen L5 and Test 3 of the round specimen L40. Both tests will be simulated in Chapter 5.

In the calibration of the material model, the equivalent stress and strain are needed. The true stress and logarithmic strain were calculated from the experimental data in section 3.4. In uniaxial tension the equivalent plastic strain p equals the logarithmic plastic strain ε_l^p . The equivalent plastic strain was found by subtracting the elastic part of the logarithmic strain from the total logarithmic strain, i.e.,

$$p = \varepsilon_l^p = \varepsilon_l - \frac{\sigma_t}{E} \quad (4.1)$$

In uniaxial tension the equivalent stress equals the true stress until diffuse necking. The formation of a neck introduces a complex triaxial stress state in that region giving an increase in the measured stress level. To find the equivalent stress after necking, the measured true stress needed to be corrected. The equivalent stress after necking was obtained using the correction proposed by Bridgman [38]

$$\sigma_{eq} = \frac{\sigma_t}{(1 + 2R/a) \ln(1 + a/2R)} \quad (4.2)$$

where a is the radius of the current cross-section of the specimen and R is the radius of the curvature of the neck. Note that the Bridgman correction is based on several assumptions. The radius a is easily measured, but estimating the radius of the curvature R can be more complicated. LeRoy et al. [39] proposed in 1981 an empirical model for the a/R ratio

$$a/R = 1.1(p - \varepsilon_{lu}^p), \quad p > \varepsilon_{lu}^p \quad (4.3)$$

where ε_{lu}^p is the equivalent plastic strain at diffuse necking. The equivalent plastic strain at diffuse necking was calculated by finding the point where the gradient of the true stress-logarithmic strain curve is equal to the true stress, i.e. the Considère criterion given as

$$\frac{d\sigma_t}{d\varepsilon_l} = \sigma_t \quad (4.4)$$

The measured data from the tension tests were a set of data points and it was impossible to apply Equation 4.4 directly since the discontinuities cause the gradient to change dramatically between each data point. A continuous differential function was obtained by curve fitting the measured data to a two term Voce rule (Equation 2.18). After calculating ε_{lu}^p , the Bridgman-LeRoy correction was applied to the experimental data after diffuse necking and the equivalent stress σ_{eq} was obtained. Figure 4.1 shows the Considère criterion and the Bridgman-LeRoy corrected equivalent stress curves for the round specimens L5 and L40. As seen in Figures 4.1b and 4.1d, the Bridgman-LeRoy corrected stress level is clearly lower than the measured stress level, indicating that the triaxial stress state arising in the neck had a significant contribution to the measured stress level after diffuse necking.

When the $\sigma_{eq} - p$ curve was calculated, the material constants in the MJC constitutive relation, see Equation 2.15, could be calibrated. The tension tests were performed at room temperature giving $T^* = 0$ and quasi-static condition means $\dot{p}^* \approx 1$. With these conditions the strain rate term in Equation 2.15 is reduced to $(1 + \dot{p}^*)^C = 2^C$. For small values of C the MJC constitutive relation becomes

$$\sigma_{eq} = (A + B^n)2^C \approx A + B^n \quad (4.5)$$

It is observed that under the given conditions the MJC constitutive relation is reduced to the Power law. If the strain hardening term in Equation 2.15 was replaced by the Voce rule under the same conditions, the equivalent stress is reduced to

$$\sigma_{eq} = \sigma_0 + \sum_{i=1}^2 Q_{Ri}(1 - \exp(-C_{Ri}p)) \quad (4.6)$$

The unknown material constants in Equation 4.5 and 4.6 were determined by the method of least squares and curve fitting in MATLAB. The material constants were fitted to the experimental $\sigma_{eq} - p$ curve until failure of the round specimens. The material constants obtained from the direct calibration are given in Table 4.1 for Power and Voce hardening laws. The constants in the MJC constitutive relation with the Voce rule are arranged so that $C_1 \geq C_2$, which implies that the first term R_1 saturates at lower strain

than the second term R_2 . Figure 4.2 shows the experimental curves along with the final calibration of both Power and Voce hardening laws.

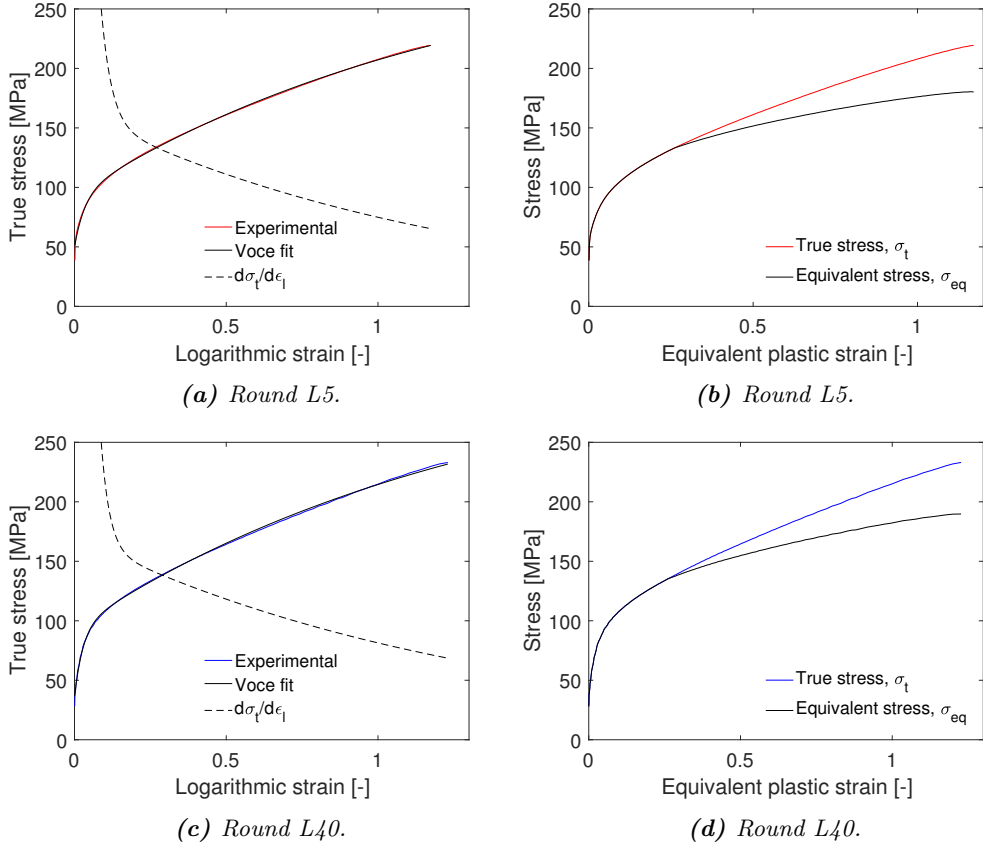


Figure 4.1: (a) and (c) Considère criterion and determination of ε_{lu}^p , (b) and (d) Comparison of the true stress-plastic strain and Bridgman-LeRoy corrected equivalent stress-plastic strain curves.

Table 4.1: Material constants of the Power and Voce hardening laws found from direct calibration.

Geometry	A [MPa]	B [MPa]	n [-]	σ_0 [MPa]	Q_{R1} [MPa]	C_{R1} [-]	Q_{R2} [MPa]	C_{R2} [-]
Round L5	7.543	169.0	0.2311	51.88	41.43	27.38	95.87	1.924
Round L40	1.579	181.7	0.2358	36.67	54.54	38.05	103.7	2.011

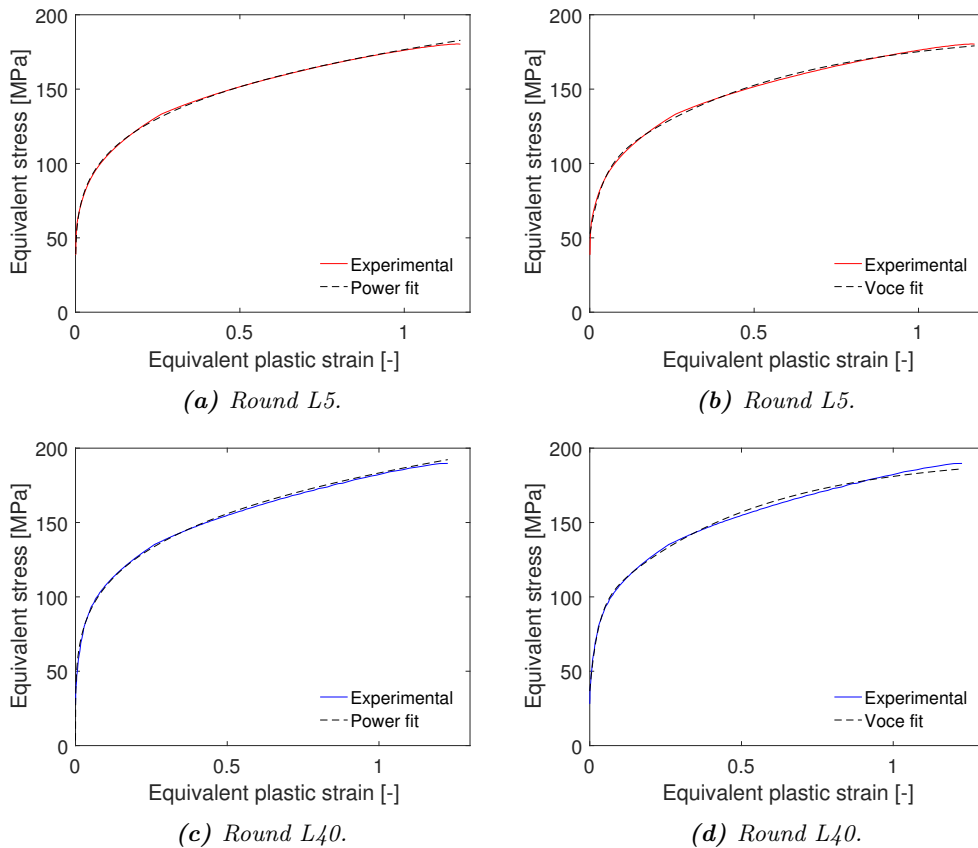


Figure 4.2: Fitted hardening laws to experimental $\sigma_{eq} - p$ curve for both geometries.

a/R -relation

LeRoy's empirical model for determination of the a/R -relation tends to give good results in combination with the Bridgman correction, as seen in e.g. [22, 40]. The model is simple to use as measurements of a and R are not needed. However, a newly implemented feature in eCorr makes it possible to determine the radius of curvature in the necked region of a specimen. The procedure of extracting the radius of curvature in eCorr is described and then the a/R -relation will be calculated and used in combination with the Bridgman's correction formula in order to compare the result with LeRoy's model. The experimental data from Test 3 of the round specimen L40 were used in this study.

Figure 4.3 shows the necked region of a specimen, marked by blue points and green lines. The minimum cross-sectional diameter is marked by the vertical pink line. The shape of the edges were interpolated with a Chebyshev polynomial function of order 30 [41], giving the green lines in Figure 4.3. Gauss weighing was used to focus the polynomial function close to the position of the minimum cross-sectional diameter. The two outer

points in the neck gave the position to where the second-derivative of the polynomial function changed sign [35]. The upper and lower radius of the curvature were obtained by fitting a circle to the two outer points using a nonlinear least squares method.

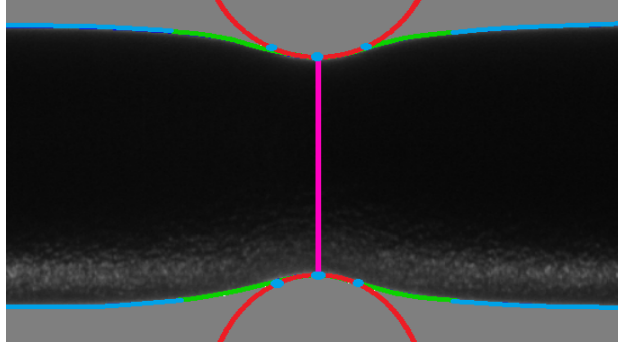


Figure 4.3: Determination of radius of curvature in the necked region of a specimen. The picture is adapted from eCorr.

At large radii of curvature, i.e. at small deformations, the search for the radius in the neck produced noise. Therefore, back-extrapolation was necessary to estimate the radius of curvature from the onset of necking, see Figure 4.4a. By applying both LeRoy's model and the eCorr-approach in Bridgman's correction formula the equivalent stresses were obtained.

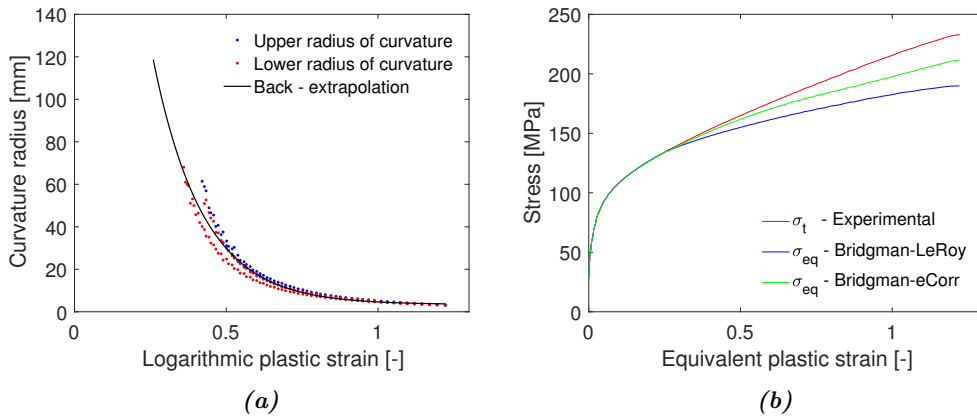


Figure 4.4: (a) Back-extrapolation of the radius of curvature, (b) Comparison of true stress and Bridgman-corrected equivalent stresses.

The two methods are compared in Figure 4.4b and a clear difference in stress level is observed, where the Bridgman-LeRoy correction estimates a lower stress level than the Bridgman-eCorr correction. As the LeRoy's model has previously given good results in combination with Bridgman correction, the Bridgman-LeRoy correction will be used in

the numerical studies in Chapter 5. However, it is important to notice the different results and that LeRoy's model is purely empirical and may not always be the best option.

The Method of Extrapolation

When performing quasi-static tension tests, extensometers are traditionally used to measure the elongation of the specimens. The use of extensometers works as long as the deformation is uniform over the whole gauge length. When diffuse necking occurs, the data from the extensometer are no longer valid. In order to evaluate the material behaviour all the way to fracture, the calculated true stress and strain have to be extrapolated to large plastic strains. A small study was performed to investigate the accuracy of the method of extrapolation.

In this investigation the direct calibration method described previous in this chapter was applied. The experimental data were taken from Test 3 of the round specimen L40. The unknown material constants of the MJC constitutive relation using both Power and Voce hardening laws, were fitted to the experimental $\sigma_{eq} - p$ curve until diffuse necking. Then, the obtained material constants were used to extrapolate the fitted curves all the way to failure. The material constants are given in Table 4.2.

Table 4.2: Material constants of the Power and Voce hardening laws found from direct calibration. The constants are fitted to the experimental $\sigma_{eq} - p$ curve until diffuse necking.

	A [MPa]	B [MPa]	n [-]	σ_0 [MPa]	Q_{R1} [MPa]	C_{R1} [-]	Q_{R2} [MPa]	C_{R2} [-]
Round L40	10.91	181.0	0.2754	33.40	82.38	4.499	44.50	59.89

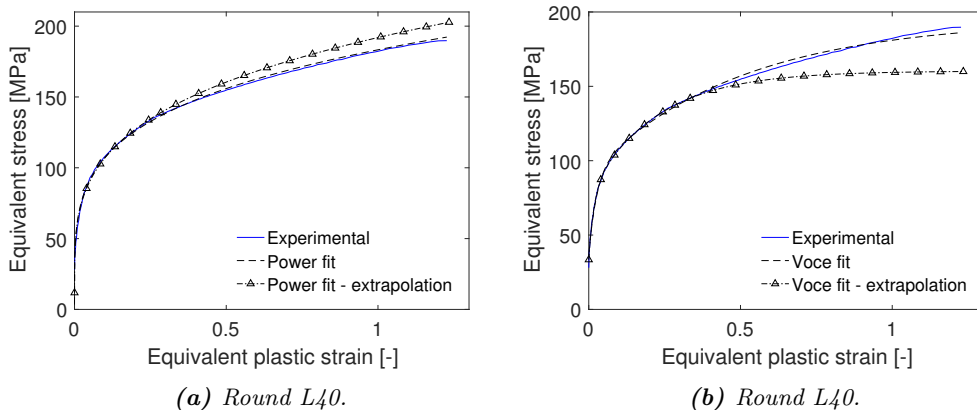


Figure 4.5: Comparison of curve fitting until fracture and curve fitting until diffuse necking and extrapolation.

Figure 4.5 compares the extrapolated curves with the experimental curves and the curves fitted to data all the way to failure (as previously). As observed, the extrapolated

curves cannot accurately describe the material behaviour from diffuse necking to failure. They follow different paths, which give a large deviation in stress level at failure. An observation of the extrapolated Voce rule is that the curve saturating to a certain stress level, which is a characteristic behaviour of the Voce hardening rule. Figure 4.5 clearly shows that the method of extrapolation is an approximation, which can lead to incorrect material behaviour at large plastic strains.

4.1.2 Flat Specimens

In Section 3.4, the true stress and logarithmic strain from the flat tension tests were calculated. However, only the data until diffuse necking were evaluated. To simulate the flat tension tests in Chapter 5, the true stress and logarithmic strain have to be extrapolated for strains beyond necking. In the calibration of the material constants in the MJC constitutive relation, the chosen representative tests were Test 1 for both the flat specimen L20 and L50.

For the flat tension tests, the true stress equals the equivalent stress as only the data until diffuse necking were considered. The equivalent plastic strain p was calculated using Equation 4.1. The tension tests of the flat specimens were performed under the same conditions as for the round specimens and the MJC constitutive relation with the Power and Voce hardening laws, given by Equation 4.5 and 4.6, respectively, were used in the direct calibration. The unknown material constants were fitted to the experimental $\sigma_{eq}-p$ curve until diffuse necking in the same manner as described for the round tension tests. The calibrated material constants are given in Table 4.3.

Table 4.3: Material constants of the Power and Voce hardening laws found from direct calibration.

Geometry	A [MPa]	B [MPa]	n [-]	σ_0 [MPa]	Q_{R1} [MPa]	C_{R1} [-]	Q_{R2} [MPa]	C_{R2} [-]
Flat L20	14.89	177.2	0.2791	39.27	37.09	59.56	76.85	5.476
Flat L50	10.00	188.3	0.2853	30.44	43.70	65.38	77.03	5.963

When the experimental $\sigma_{eq}-p$ curves were fitted until diffuse necking, the obtained material constants were used to extrapolate the fitted curves. The plastic strain region was expanded to 150 %. The extrapolated $\sigma_{eq}-p$ curves for the flat specimens are presented in Figure 4.6. As observed, the extrapolated curves give two very different material behaviours. As discussed above, the method of extrapolation is an approximation and extrapolated curves might not be able to describe the exact material behaviour from diffuse necking to fracture. Both hardening laws will be used in the simulations of the flat tension tests in Chapter 5.

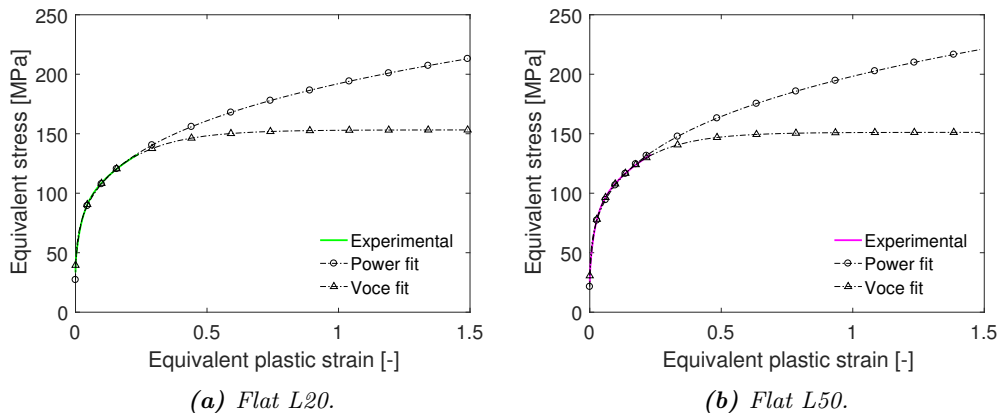


Figure 4.6: Fitted hardening laws to experimental $\sigma_{eq} - p$ curve for the flat tension tests. The curves are extrapolated from diffuse necking.

4.2 Calibration of Fracture Model

A fracture criterion is required to predict fracture in numerical simulations. In order to calibrate the JC fracture criterion, more extensive material tests are required, e.g. quasi-static tension tests of notched specimens. As the material tests performed in this thesis were limited to quasi-static tension tests of round specimens, there were not enough data to determine the constants in the JC fracture criterion. Hence, only the CL fracture criterion will be applied in this thesis.

The CL fracture criterion, see Section 2.3.2, says that fracture is assumed to occur when the damage variable $\omega = 1$. The only unknown model constant was the fracture parameter W_c which, for a uniaxial tension test, can be estimated as the integral of the true stress with respect to the true plastic strain up to fracture, see Equation 2.21. From the tension tests of the round specimens, the experimental true stress and true plastic strain were calculated and the fracture parameter was approximated by numerical integration. The values of W_c , given in Table 4.4, were estimated from the experimental results of Test 4 of the round specimen L5 and Test 3 of the round specimen L40.

Table 4.4: The fracture parameter W_c estimated from the experimental results of the round tension tests.

	Round L5	Round L40
	[MPa]	[MPa]
Experimental W_c	192.8	210.7

5 | Numerical Work

5.1 Direct Calibration

The quasi-static tension tests performed in this thesis were recreated and analysed using ABAQUS/Standard in order to verify the material models calibrated in Chapter 4.

The von Mises yield criterion and the associated flow rule were chosen by default in all the numerical models in this Chapter. The mass density ρ and the Poisson's ration ν for aluminium were given as $\rho = 2.7 \text{ g/m}^3$ and $\nu = 0.3$, respectively. These values are typical values for aluminium taken from the literature. The determination of the Poisson's ratio requires special tests, which were not performed in this thesis.

5.1.1 Round Tension Tests

The round tensile specimens were modelled using 2D axisymmetry and symmetry in the longitudinal direction. This simplification was made to save computational time. The 2D axisymmetric models are known to give good results, however a 3D model was also modelled to compare the two approaches. The nominal geometries shown in Figure 3.1 were used in the models. The threaded ends were excluded in the models as they have no effect on the results.

To optimize the models, a small sensitivity study was performed. The influence of mesh size was investigated by running simulations with three mesh densities. The element sizes in the gauge region of the specimens were $0.5 \times 0.5 \text{ mm}^2$, $0.3 \times 0.3 \text{ mm}^2$ and $0.1 \times 0.1 \text{ mm}^2$. The results showed that the mesh size had an influence on the numerical stress-strain curves at failure and, compared with the experimental curves, the element size of $0.1 \times 0.1 \text{ mm}^2$ gave the best result for both specimen geometries. The round specimens were meshed with 4-node bilinear axisymmetric quadrilateral elements (CAX4) with full integration. Figure 5.1 shows the mesh of the round tensile specimens. Both specimens had a coarser mesh outside of the gauge region. As the models experience only tensile forces, fully integrated elements will not cause any problems regarding shear locking. Both fully and reduced integrated elements have been analysed and there was no difference in the results. Therefore, fully integrated elements were chosen to increase the accuracy of the numerical integration process.

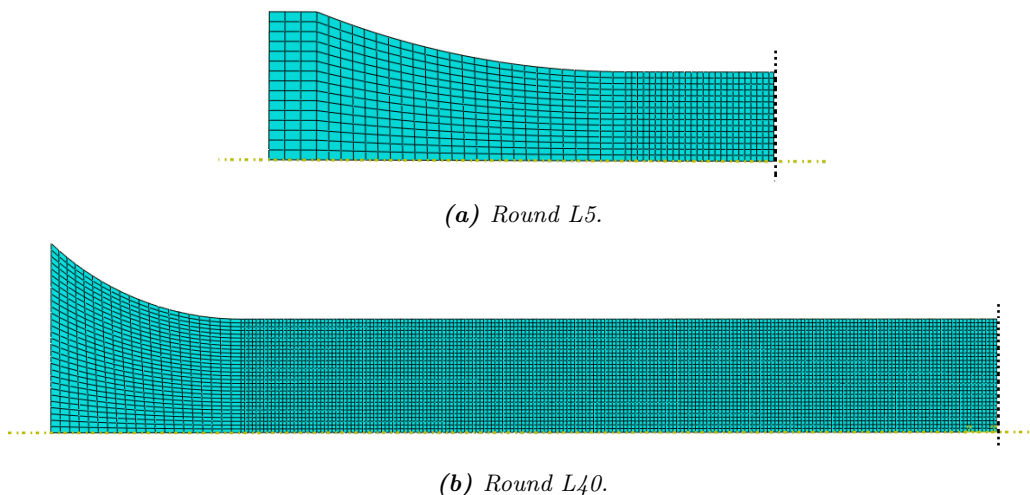


Figure 5.1: Mesh of the round tensile specimens. The dashed lines symbolize the axisymmetry (yellow) and symmetry (black) axes.

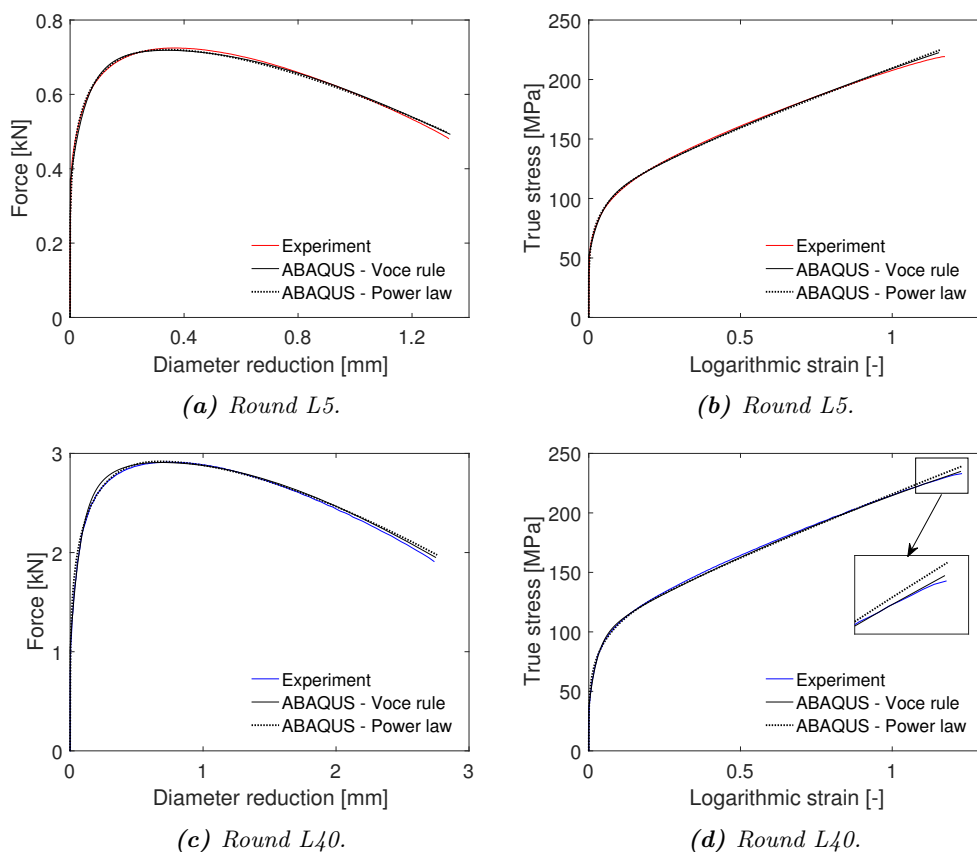


Figure 5.2: The results from the numerical simulations of the round specimens based on the direct calibration. Force-diameter reduction (left) and true stress-logarithmic strain (right).

The JC constitutive relation and the JC fracture model are both available in ABAQUS, while the MJC constitutive relation and the CL fracture model are not. However, the MJC constitutive relation with both Power and Voce hardening laws were included in the material cards of the models, where the equivalent plastic strains and equivalent stresses were tabulated. Fracture was not evaluated in this case, therefore an implicit solver in ABAQUS was used in the numerical models. In ABAQUS/Standard fracture criteria are not available. The tensile force was applied on the left end of the specimens and was given as a constant displacement of 1.75 mm and 7.5 mm for the round specimen L5 and L40, respectively. The constant displacements corresponded to half of the total displacement of the specimens from the experiments due to the symmetry conditions. To extract data from the simulations, the diameter reduction at the neck and the applied force were reported. From this, the true stress and logarithmic strain were calculated. The results from the simulations are given in Figure 5.2. As seen, the two hardening laws represent the material behaviour in a good way. The Voce rule is a slightly better match at large plastic strains for the round specimen L40, as seen in Figure 5.2d. The simulations agree nicely with the experiments and hence the direct calibration predicts the material behaviour well in this case.

The deformed shape of the round specimens from the experiments and the numerical models of the corresponding specimens are visually shown in Figures 5.3 and 5.4. It is observed that the deformed shape from the experiment is well represented by the numerical model for both specimen geometries.

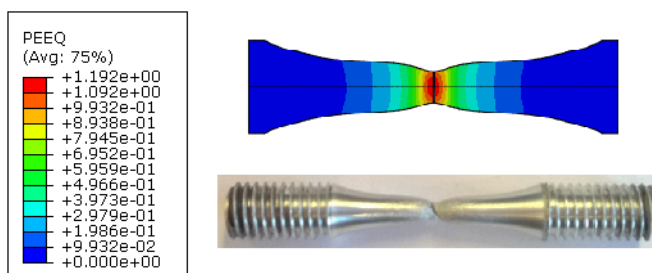


Figure 5.3: Visual representation of the deformed shape of the experimental and the numerical model specimens. Note that the threaded part is not included in the numerical model and that the geometry is mirrored. PEEQ is the equivalent plastic strain.

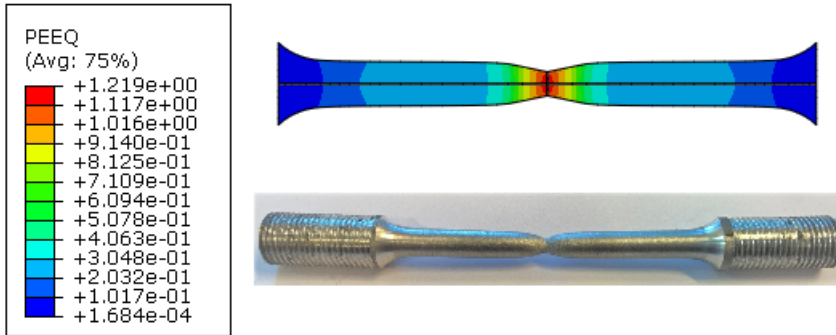


Figure 5.4: Visual representation of the deformed shape of the experimental and the numerical model specimens. Note that the threaded part is not included in the numerical model and that the geometry is mirrored. PEEQ is the equivalent plastic strain.

3D Model

A 3D model of the round specimen L5 was created in ABAQUS/Implicit using 360° revolution. The specimen was meshed with 8-node linear brick elements (C3D8) with full integration and the mesh size in the gauge region was set to $0.1 \times 0.1 \text{ mm}^2$. Figure 5.5 shows the mesh of the 3D model. The MJC constitutive relation with Voce hardening rule was used and the specimen was fixed at one end due to that the hole length was modelled, else the 3D model was modelled as the axisymmetric model. The results from the simulations showed that there was no significant difference between the true stress-logarithmic strain curves for the axisymmetric model and the 3D model. However, the total computational time is an important factor as the axisymmetric model was approximately 300 times faster than the 3D model. The heavy computational time of the 3D model makes the axisymmetric model the best choice in this case.

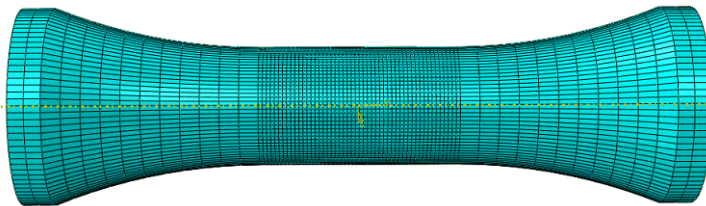


Figure 5.5: The mesh of the 3D model of the round specimen L5. Note that the threaded ends are not included in the numerical model.

5.1.2 Flat Tension Tests

The numerical models of the flat tensile specimens were simplified by using symmetry in the longitudinal, the transverse and the thickness directions. These simplifications were made to save computational time. The nominal geometries used in the simulations are shown in Figures 3.2 and 3.3. The circular holes in the specimens were not included in the numerical models.

The specimens were modelled with 3D solid elements. The models were partitioned into three main parts in order to make the mesh more structured. A small sensitivity study on the mesh size in the gauge region was performed. The element sizes of $0.5 \times 0.5 \text{ mm}^2$, $0.25 \times 0.25 \text{ mm}^2$ and $0.1 \times 0.1 \text{ mm}^2$ were studied for the flat specimen L20. The results showed that there was no significant influence of mesh size for the two refined meshes on the numerical stress-strain curves before diffuse necking, therefore the element size of $0.25 \times 0.25 \text{ mm}^2$ was used to save computational time. For the flat specimen L50 on the other hand, the element size of $0.5 \times 0.5 \text{ mm}^2$ gave accurate results and was therefore used in the simulations. The specimens were meshed with 8-node linear brick elements (C3D8) with full integration. The mesh of the flat tensile specimens are shown in Figure 5.6.

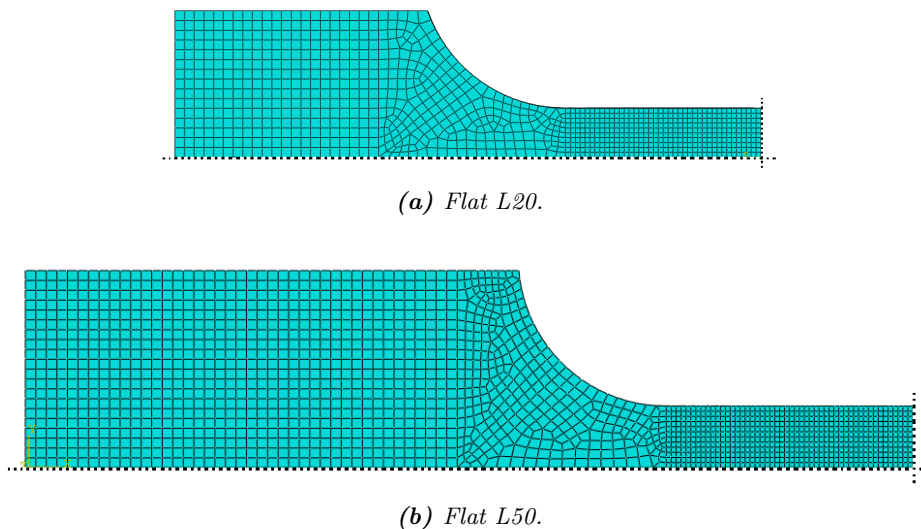


Figure 5.6: Mesh of the flat tensile specimens. The black dashed lines symbolize the symmetry planes.

The material inputs were the same as for the round specimens. The tensile force, applied on left end of the specimens, was given as a constant displacement of 5 mm and 12.5 mm for the flat specimen L20 and L50, respectively. The elongation of the specimens was reported from two single nodes. One was placed at approximately the same position as the extensometer clip arms and the other had approximately the same position as the vector from the DIC analyses. The results from the simulations are given in Figure 5.7.

As observed in Figures 5.7a and 5.7c the simulations agree nicely with the experiments and the direct calibration predicts the correct material behaviour in this case. However, the Voce rule predicts the maximum engineering stress at a lower strain than the experiments and the necking point, marked by a black o, appears at lower a strain level. In Figures 5.7b and 5.7d, the elongation from the extensometers are compared with the simulations and, as observed, the curves coincide to a certain degree and the stress level at diffuse necking is about the same. For both specimens, a difference in the strain level at diffuse necking is observed for the two hardening laws, which is especially visible for the Power law in Figure 5.7d.

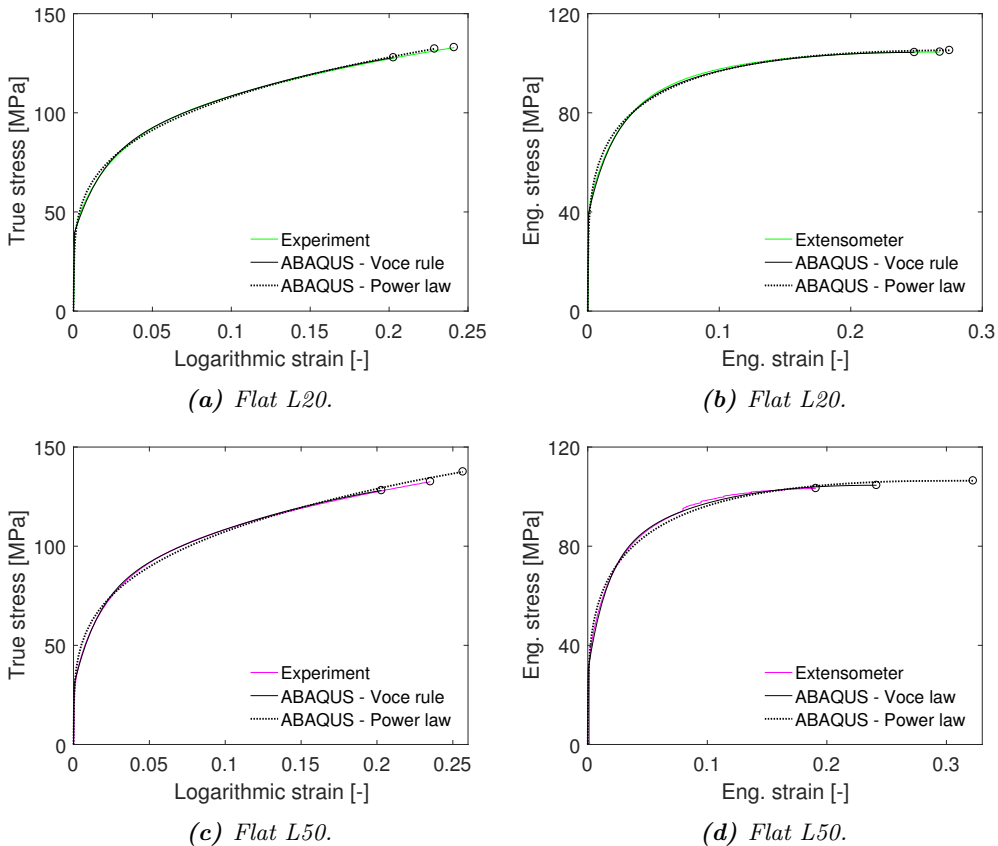


Figure 5.7: Results from the numerical simulations using the direct calibration of the Voce and Power hardening laws as input data in ABAQUS. The results are compared with the experimental data. The black o indicates diffuse necking. True stress-logarithmic strain curves (left) and engineering stress-strain curves from the extensometer (right).

The deformed shape of the flat specimens from the experiments and the numerical models of the corresponding specimens are visually shown in Figures 5.8 and 5.9. It is observed that the deformed shape from the experiment is well represented by the

numerical model for the flat specimen L20. As seen in Figure 5.4, necking of the specimen from the experiment is not in the centre of the specimen, but slightly to the left. This may be due to that there was a small imperfection in the material in that point. Imperfections have not been included in the numerical analyses and diffuse necking occurs in the centre of the model as expected.

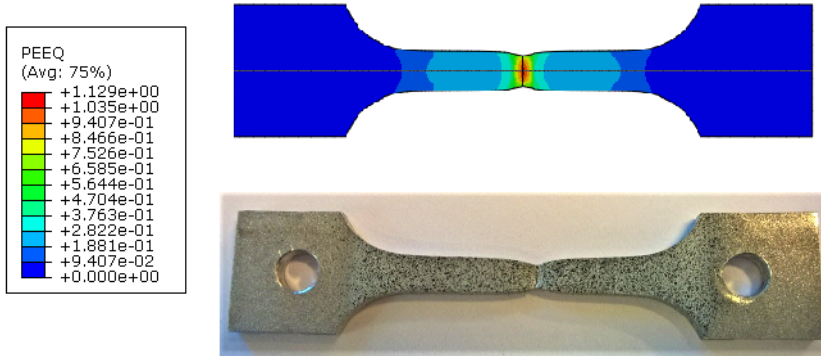


Figure 5.8: Visual representation of the deformed shape of the experimental and the numerical model specimens. Note that for the numerical model the geometry is mirrored. PEEQ is the equivalent plastic strain.

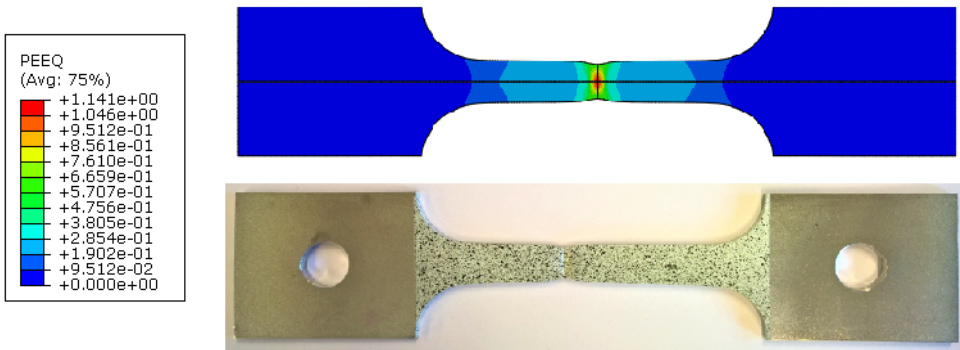


Figure 5.9: Visual representation of the deformed shape of the experimental and the numerical model specimens. Note that for the numerical model the geometry is mirrored. PEEQ is the equivalent plastic strain.

Parametric Study

The results from the simulations of the 3D models of the flat tension tests corresponded very well with the experimental results. However, in the making of the models some choices and simplifications were made. The circular holes in the specimens were excluded from the analyses and 3D models were created instead of 2D models, which requires

more computational time. These parameters were investigated to study the effects on the results.

A 3D model of the flat specimen L20 created with circular holes at each end of the specimen was provided by PhD Candidate Henrik Graunm at SIMLab [42]. By including the circular holes in the numerical model, the boundary conditions from the experiment were more accurately represented. Except from the circular holes, the 3D model was created in the exact same way as the 3D model created in Section 5.1.2. The circular holes had a diameter of 5 mm. The specimen was loaded through a rigid pin modelled as a discrete surface. The contact was assumed frictionless. Figure 5.10 shows the deformed shape of the numerical model with the equivalent plastic strain distribution along the specimen. The results from the simulations showed that the circular holes had no influence on the true stress-logarithmic strain curves until diffuse necking, hence the holes have negligible effect on the deformation in the gauge area and could be excluded from the models. In computational time, the 3D model created with the circular holes takes approximately 17% longer time than the 3D model created without the circular holes.

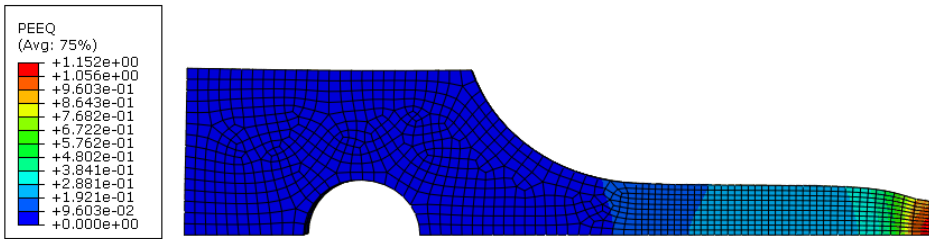


Figure 5.10: Deformed shape of the numerical model of the flat specimen L20 with a circular hole. PEEQ is the equivalent plastic strain.

The 2D models of the flat specimens were created using deformable shell elements with a plane stress thickness of 3 mm, which is the nominal thickness of the specimens. Symmetries in the longitudinal and transverse directions were also used to save computational time. The element size in the gauge region of the flat specimens L20 and L50 were $0.25 \times 0.25 \text{ mm}^2$ and $0.5 \times 0.5 \text{ mm}^2$, respectively. Figures 5.11 and 5.12 show the mesh of the 2D models, where 4-node bilinear plane stress quadrilateral elements (CPS4) with full integration were used. The MJC constitutive relation with Voce hardening rule was used and the boundary conditions were the same as for the 3D models.

The results from the simulations of the 2D models gave exactly the same results as for the 3D models. This indicates that the 2D models are as good as the 3D models in this case. By looking closer at the total computational time, the simulations of the 3D model take approximately 90 % longer time than the 2D model for the flat specimen L20, while for the flat specimen L50 the 3D model takes approximately 87 % longer time than the 2D model. This clearly shows that the 2D models have an advantage when it comes to computational time and, as there was no difference in the result, the 2D models can describe the material behaviour of the flat tension tests accurately. The 2D models were further used in the inverse modelling in Section 5.2.

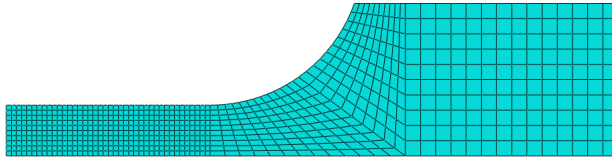


Figure 5.11: Mesh of the 2D model of the flat specimen L20.

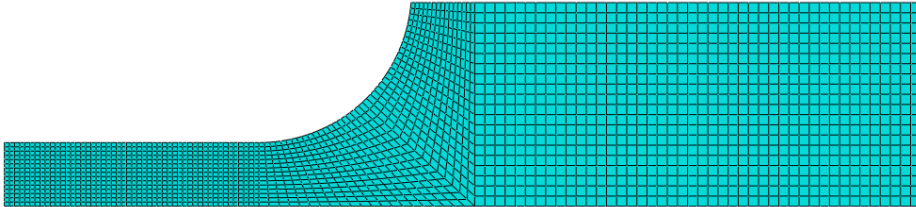


Figure 5.12: Mesh of the 2D models of the flat specimen L50.

5.2 Inverse Modelling

Inverse modelling is a calibration method that uses a trial and error approach that tunes the constants of a material model until the material model predicts the experimental material behaviour well. This process of trial and error is cumbersome when done by hand and can be highly simplified when using a numerical optimization tool.

The numerical optimization tool used in this thesis was the design optimization code LS-OPT [37]. LS-OPT interacts with the finite element code LS-DYNA [43], but in the LS-OPT setup ABAQUS can be specified as a user-defined solver. One drawback with the numerical optimization process is that it can be time consuming, especially for complex hardening laws with many material parameters to be determined and for computationally heavy FE-models.

The inverse modelling process was as following. Before running the optimization analyses, numerical models of the tensile specimens had to be created in ABAQUS. LS-OPT read the ABAQUS input-file, together with a separate input file containing information on the material parameters to be optimized. Based on this, LS-OPT ran several iterations while changing only the desired parameters to obtain the solution with the smallest mean square error between a target curve and the computed curve.

The numerical models of the tension tests created in Section 5.1 were used in the inverse modelling. The models of the round tension tests are axisymmetric which is beneficial compared to e.g. a 3D model since a high number of analyses have to be run during each optimization. For the flat tension tests, the 2D models created in Section 5.1.2 were used instead of the 3D models to save computational time. The measured force-diameter reduction curves from the tests were used as the target curves for the round specimens, while the target curves for the flat specimens were the engineering stress-strain curves. The curves were discretized into 100 data points before the optimization,

otherwise no other manipulations were performed (e.g. weighting). The optimization was run using the MJC constitutive relation with the two term Voce hardening rule given as

$$\sigma_{eq} = \sigma_0 + R(p) = \sigma_0 + \sum_{i=1}^2 Q_{Ri}(1 - \exp(-\theta_{Ri}(p))) \quad (5.1)$$

where $\theta_{Ri} \equiv Q_{Ri}C_{Ri}$ is the work-hardening rate. Q_{R1} , θ_{R1} , Q_{R2} and θ_{R2} were material parameters that could be changed to obtain the best fit, while σ_0 was held constant. The material parameters obtained from the direct calibration were used as initial values. A cut-off-criterion was included in LS-OPT which terminated the optimization after 30 iterations.

Some adjustments could be necessary during the iteration process. A narrow solution range should be defined for the variables so that LS-OPT will not start to search for a local mean square error minimum instead of a global mean square error minimum. However, if one of the optimized parameters is equal the limit value, the solution range might be too narrow and should be expanded to get a better fit. This process demands some trial and error.

Table 5.1 shows the optimized material parameters compared with the material parameters obtained from the direct calibration.

Table 5.1: The obtained direct calibrated and inverse modelled material parameters for the four specimen geometries.

Geometry	Method	Q_{R1} [MPa]	θ_{R1} [-]	Q_{R2} [MPa]	θ_{R2} [-]
Round L5	Optimized	31.64	1362.58	90.13	272.43
	Dir. Cal.	41.43	1134.35	95.87	184.45
Round L40	Optimized	43.06	2196.74	95.40	308.12
	Dir. Cal.	54.54	2075.25	103.7	208.54
Flat L20	Optimized	37.92	2451.40	82.13	395.46
	Dir. Cal.	37.09	2209.28	76.85	420.78
Flat L50	Optimized	49.29	2951.48	86.79	352.00
	Dir. Cal.	43.70	2857.12	77.03	459.33

The round specimen L5 gave good results after using LS-OPT and all the four material parameters converged. The same applied for the round specimen L40. The results from LS-OPT, see 5.13a, shows how the optimal force-diameter reduction curve approaches the target curve for the round specimen L5. From this figure, it is evident that a good solution was reached after about nine iterations. Figure 5.14a shows how Q_2 converges from the directly calibrated value to the optimized value. The flat specimens gave also a good fit, as shown in Figure 5.13b for the flat specimen L50. As seen in the figure, a good solution was obtained after approximately 13 iterations. However, the convergence of the parameters was more difficult. The Q_2 had problems converging for the flat specimen L50, see Figure 5.14b.

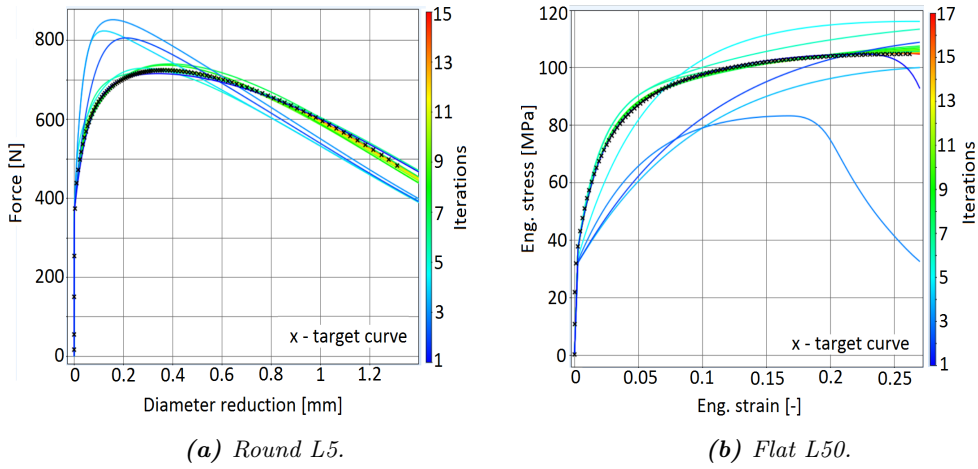


Figure 5.13: Screenshots from LS-OPT where only the best computed iterations are displayed.

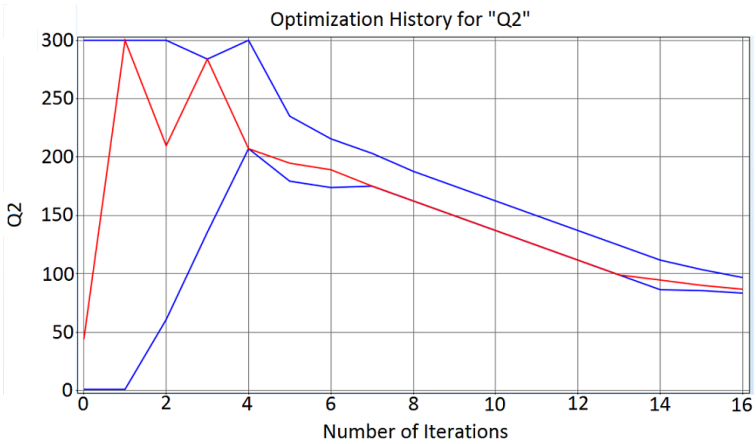
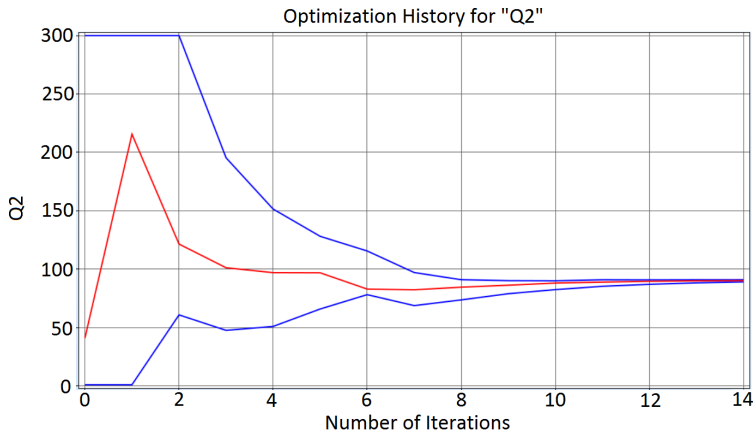


Figure 5.14: Screenshots from LS-OPT showing how Q_2 converges well for the round specimen L5 and has problems converging for the flat specimen L50.

Figure 5.15 compares the equivalent stress-strain curves obtained from the direct calibration and the inverse modelling. As seen in Figures 5.15c and 5.15d, the optimized material parameters from the inverse modelling of the flat specimens corresponded very well with the direct calibration method, even though some of the parameters had trouble converging. For the round specimens on the other hand, Figures 5.15a and 5.15b show that the inverse modelling resulted in a lower stress level at large plastic strains compared with the direct calibration. In Section 5.1, the results showed that the direct calibration corresponded well with the experimental results. Hence, the inverse modelling of the round specimens could not predict the material behaviour very well at large plastic strains in this case. In order to get a better fit, further trial and error of different user-defined parameters in LS-OPT could have been carried out.

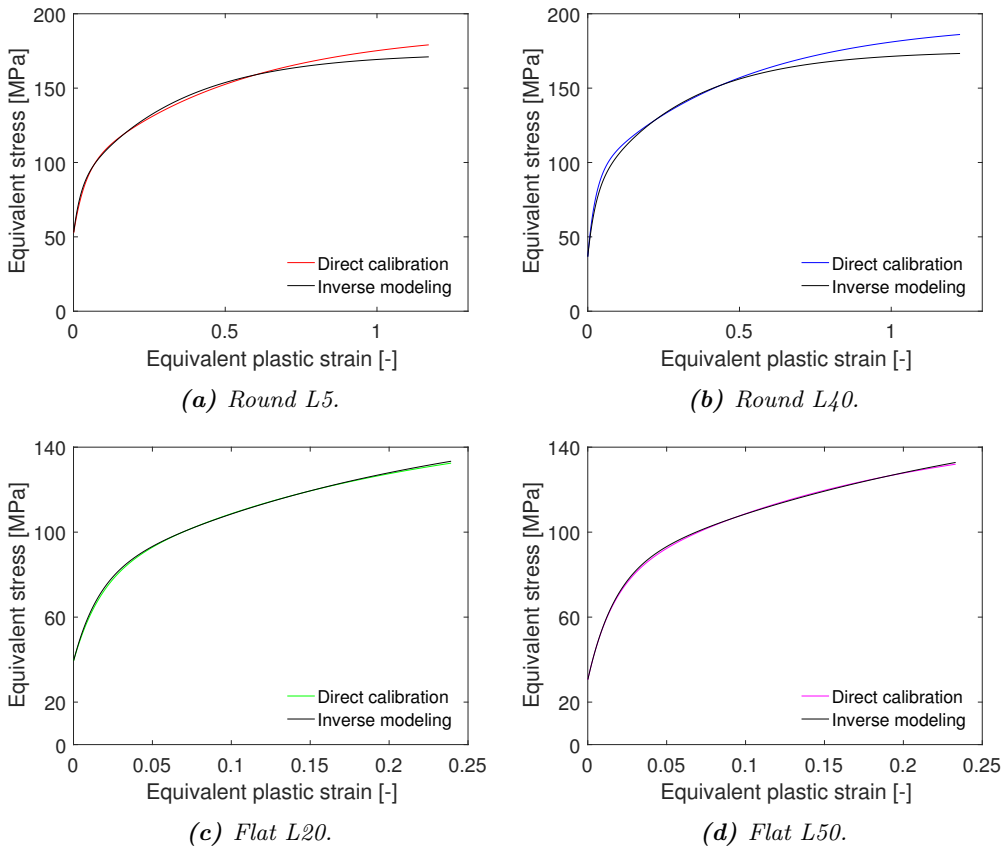


Figure 5.15: Equivalent stress-strain curves from the inverse modelling compared with the direct calibration.

As mentioned, there are several user-defined parameters in LS-OPT which the user must select. The different user-defined parameters can influence both the efficiency of the optimization procedure as well as the result of it. There are several experimental design

criteria available and the so-called D-optimality criterion was chosen in this thesis, which is the default method in LS-OPT. In addition, the order of polynomial approximation could be changed, where a high-order polynomial approximation yields a better accuracy and faster convergence than a lower-order approximation. However, a high-order approximation takes more computational time [44]. In this case, a first-order polynomial approximation was used.

All the possibilities in LS-OPT have not been employed in this thesis and further trial and error with different parameters could give better results. However, optimization is time consuming and the obtained results are considered sufficient.

5.3 DIC-FEM

A novel technique, which is still under development, incorporates Digital Image Correlation (DIC) and the Finite Element Method (FEM) in a coupled approach (Fagerholt et al. [45]). The aim of this approach is to obtain optimized material properties based on rather simple material tests.

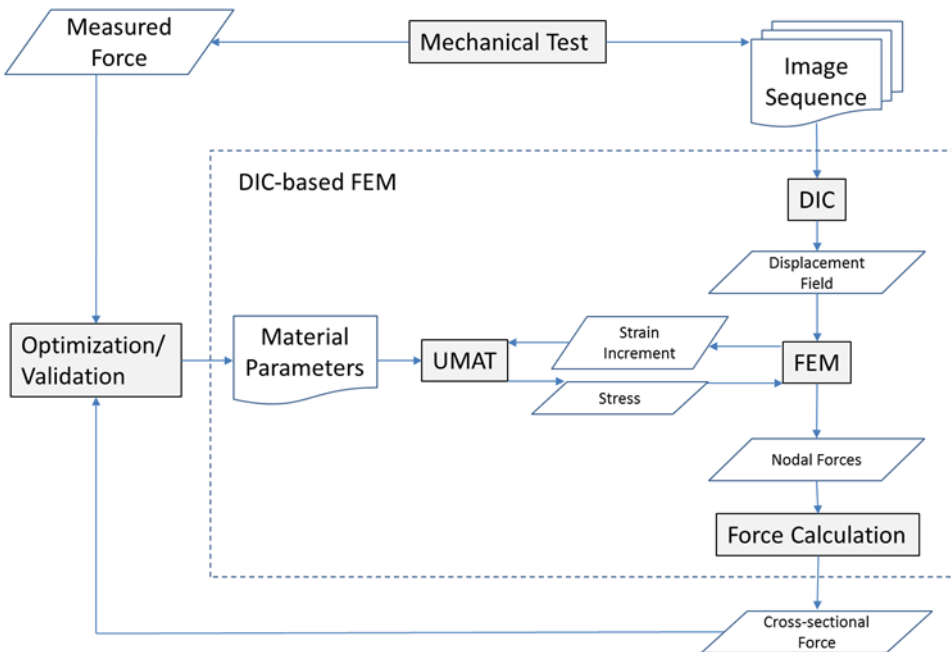


Figure 5.16: A schematic overview of the proposed DIC-based FEM approach with optimization of material parameters. The figure is adapted from Fagerhold et al. [45].

A schematic overview of the DIC-based FEM approach is given in Figure 5.16. By using two-dimensional DIC in a mechanical test, the in-plane displacement and strain

fields are easily measured from images of a single camera. The displacement field is the input data in the FEM routine.

In the FEM routine, the stresses, internal variables and nodal forces are computed using constitutive models. The global force is calculated by integrating the nodal forces over the selected cross-section, transverse to the loading direction. The calculated global forces are compared to the recorded global forces from the test. Thus, the calculated and measured global force values provide a basis for optimization and validation of the material model and the associated material parameters. The reader is referred to Fagerholt et al. [45] for more details on the algorithms behind this DIC-based FEM approach.

The DIC-based FEM approach was performed on the flat specimen L50. The resulting image sequence obtained from the test was processed using the in-house DIC code eCorr. In eCorr, see Figure 5.17, a structural Q4 mesh was generated over the necked region of the specimen. The mesh should cover the hole width of the specimen in order to extract information at the edges. A strain field was then obtained from a single row of elements, see Figure 5.17b.

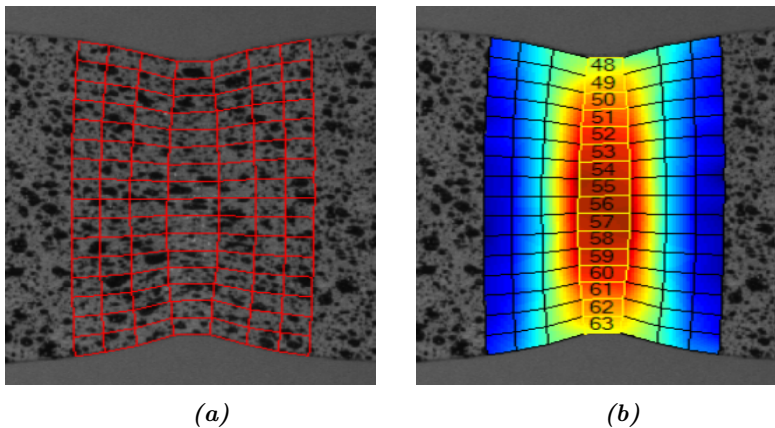


Figure 5.17: Screenshots from eCorr. (a) Structured Q4 mesh over the necked region, (b) Field map showing the principal strain in the longitudinal direction.

To avoid noise, filtering of the DIC data was carried out. A two-step procedure of filtering the DIC results were performed. First, a time-moving average filter which acted on each node separately and smoothed its displacement in time. Second, a spatial filter with Gauss weighting which acted on the nodal displacements for a particular time step and smoothed the displacement in the image plane. The radius of pixels was set to 25 (default value). With these filters the DIC data became smooth and were further sent as input to the finite element routine.

In this thesis, only the DIC part of the DIC-FEM approach was carried out due to that the FEM routine is still under development. The FEM routine is proposed as further work.

6 | Numerical Case Study: Component Test

In this thesis, uniaxial tension tests were performed on both round and flat specimens which gave a solid basis for identifying the mechanical properties of an aluminium alloy. Often, in e.g. the car industry, the mechanical properties of metals are based on tension tests of flat, dog-bone shaped specimen due to limitation in the design geometries (e.g. design of thin plates) [46]. The experimental data from flat tension tests are only valid until diffuse necking and extrapolation is necessary. Therefore, in this case study, the obtained data from the tension tests of the round and flat specimens were used as input data in a component test to investigate the difference between data that were curve fitted all the way to failure (round specimens) and data that were extrapolated from diffuse necking (flat specimens).

The component test chosen for this purpose was a quasi-static compression test of a rectangular, thin-walled tube. The numerical model was provided by PhD Candidate Henrik Granum from SIMLab [42].

The numerical model was established in ABAQUS/Explicit using 3D solid elements. The nominal dimensions of the tube are given in Appendix A.2. The tube was meshed with 8-node linear brick elements with reduced integration (C3D8R) where hourglass control was activated in order to avoid zero-energy modes. The global element size was set to $1.0 \times 1.0 \text{ mm}^2$. Two 3D analytical rigid plates were created in order to accurately represent the boundary conditions of the test machine. One of the plates was given a constant velocity and time scaling was used to reduce the computational time, while the other plate was fixed. Friction between the rigid plates and the tube was included in the model, in addition to self-contact due to the specific folding mechanisms of the tube. Finally, it was checked that the kinetic energy remained negligible compared with the internal energy of the tube during the deformation process.

The material was modelled with the von Mises yield criterion, the associated flow rule and isotropic hardening. The MJC constitutive relation with the Voce hardening rule was included in the material card, where the equivalent stresses and equivalent plastic strains were tabulated. A fracture criterion was not included or considered in this case. The input data were from the representative tests of the round specimen L40 and the flat specimen L20.

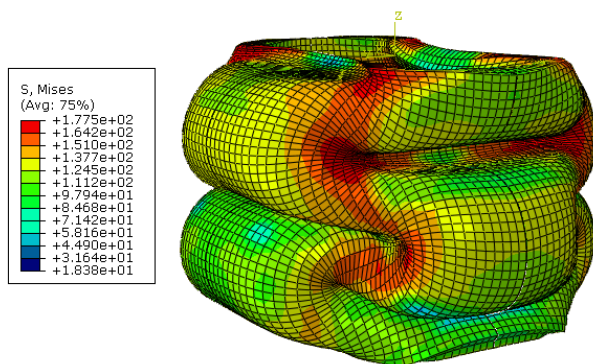


Figure 6.1: Deformed shape of the tube.

The deformed shape of the tube and the results from the simulations are given in Figures 6.1 and 6.2, respectively. The tube deformed until the equivalent plastic strain in one of the most loaded elements was approximately 150 %, i.e. the tube experienced large plastic strains. As seen in the force-displacement diagram in Figure 6.2a, the curves for the round and flat tension tests using the Voce rule give the same response and agree very well. The results from the simulations demonstrated that measured data from a round tension test and a flat tension test can both give the same material behaviour in nonlinear structural problems with large plastic strains.

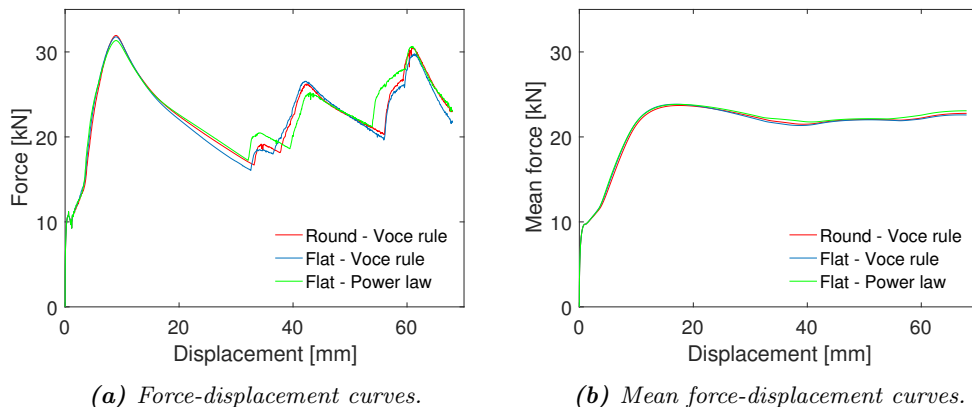


Figure 6.2: The results from the simulations of the quasi-static compression test.

The results from the flat tension test using the Power law has a small deviation after the first peak, compared with the Voce rule as seen in Figure 6.2a. By considering the first peak in the force-displacement diagram, the difference between the Voce and Power hardening laws are negligible (only about 1.4 %). As the tube is deforming, the difference

between the two hardening laws is increasing and the biggest difference is located between the second and third fold, corresponding to the second and third peak in Figure 6.2a. At that point the difference in force level is about 7 MPa, corresponding to about 25 %. In Figure 6.2b the mean force-displacement curves are displayed. The three curves coincide, hence the models absorb approximately the same amount of energy throughout the simulations.

The aim of this case study was to check that the material properties obtained from the round and flat tension tests gave the same result in a nonlinear finite element simulation with large plastic strains. The study showed that the two tension tests resulted in approximately the same material behaviour, regardless of whether the data were curve fitted all the way to failure or extrapolated from diffuse necking.

7 | Concluding Remarks

The main objective of this thesis was to investigate the reliability of the material properties obtained from uniaxial tension tests of small versus large round specimens and small versus large flat specimens, in addition to comparing the accuracy of different measurement techniques. Uniaxial tension tests have been carried out with four specimen geometries in order to identify the mechanical properties of the material. The tests have been conducted using different measurement techniques such as extensometer, laser micrometer, Digital Image Correlation (DIC) and edge tracing. The experimental data have been processed and the modified Johnson-Cook (MJC) constitutive relation and the Johnson-Cook (JC) fracture criterion were calibrated based on the experimental results. The material tests were further numerically simulated using ABAQUS/Standard in order to verify the calibrated material models. In addition, the results from inverse modelling were compared with the direct calibration. Finally, the experimental data were used in a numerical case study to investigate if the different input data had significant effect on the results in more complex nonlinear structural problems.

Experimental Work

With the use of different measurement techniques, the user-friendliness and accuracy of the methods were compared. Prior to the tests, all the specimens were measured. The laser micrometer measured the initial diameters in situ with a high accuracy while for the edge-trace and DIC approaches the initial dimensions were manually measured with a digital slide gauge, which has a lower accuracy than the laser. It was observed that the accuracy of the measured initial dimensions influenced the calculated stress level. An inaccuracy of 0.05 mm in initial diameter lead to a deviation in stress at failure of 10 MPa. This clearly showed that accurate measurements of the initial dimensions of the specimens were very important. For an untrained user, some guidelines of how to use a digital slide gauge could get rid of some of the gross errors and lead to more accurate measurements.

The results from the tension tests of the round and flat specimens showed that there was a good repeatability within each geometry and each method. However, when the results from the round and flat specimens were compared, a deviation between the round specimen L5 and the three other specimen geometries was clearly observed. The results from the new tests gave also the same deviation. The reason of this deviation of the round

specimen L5 is unknown, but it is speculated that this can be a scalar effect since the round specimen L5 has clearly the lowest cross-sectional area in the loading direction of the four specimen geometries.

The measured data from the flat specimens were only evaluated until diffuse necking in this case. Comparison of the edge-trace and DIC approaches showed that the two approaches gave the same results until diffuse necking. However, for large strains the measured data from the flat specimens had to be extrapolated, which lead to considerable deviation. This meant that when DIC was used as an optical extensometer in this case, the approach cannot be used to investigate fracture. The results from the extensometers validated that the measured data from the edge-trace and DIC approaches gave the correct response.

Numerical Work

The numerical models of the tension tests were used to validate the direct calibrated constants in the MJC constitutive relation and to optimize the constants with inverse modelling. The results based on the direct calibration corresponded very well with the experimental results. This showed that the direct calibration predicted the material behaviour well, at least of this material.

From the inverse modelling process, the optimized model constants for the flat specimens corresponded very well with the direct calibration and hence the experimental results. For the round specimens, the optimized constants resulted in a slightly lower stress level at large plastic strains than the direct calibration. Since the direct calibration corresponded well with the experimental results, the inverse modelling could not predict the material behaviour well at large plastic stains in this case. The reason for this deviation for the inverse modelling is not known and further optimization by changing the parameters in LS-OPT could result in a better fit.

Numerical Case Study

A numerical case study of a structural component was performed in order to check that the obtained data from the round and flat tension tests gave the same response in a nonlinear finite element simulation. The results showed that the data from the round and flat tension tests, using the MJC constitutive relation with Voce hardening rule, gave the same global response. The data from the flat tension test using the MJC constitutive relation with the Power hardening law resulted in similar behaviour, but a small deviation was observed after the first peak. This study demonstrated that the data from round and flat tension tests resulted in the same behaviour in a complex nonlinear structural problem in this case. In conclusion, the tension tests of round and flat specimens are both valid for identification of reliable mechanical properties of materials.

8 | Further Work

Based on the work done in this thesis some suggestions of further work are here proposed.

- Carry out the same tests performed in this thesis on a 6XXX series aluminium alloy, where the result from the tests could be compared with the nanostructure model, NaMo. This could also have been performed using steel.
- Study the DIC-FEM approach in more details and perform the FEM routine when the routine is fully developed.
- More extensive analyses in LS-OPT while changing the user-defined parameters in an attempt to get a better fit for the round specimens.
- Numerical simulations of the round tension tests in ABAQUS/Explicit in order to include the CL fracture criterion.
- More extensive tests of the round specimen L5 in an attempt to find a reason for the deviation at yielding.

Bibliography

- [1] M. S. Loveday, T. Gray, and J. Aegerter, “Tensile testing of metallic materials: A review,” *Final report of the TENSTAND project of work package*, vol. 1, 2004.
- [2] E. W. Hart, “Theory of the tensile test,” *Acta Metallurgica*, vol. 15, no. 2, pp. 351–355, 1967.
- [3] J. M. Holt, *Uniaxial Tension Testing, Mechanical Testing and Evaluation*, vol. 8. ASM International, Materials Park, OH, 2000.
- [4] W. F. Hosford and R. M. Caddell, *Metal forming: mechanics and metallurgy*. Cambridge University Press, 2011.
- [5] J. R. Davis, *Tensile testing*. ASM international, 2004.
- [6] J. W. House and P. P. Gillis, *Testing Machines and Strain Sensors, Mechanical Testing and Evaluation*, vol. 8. ASM International, Materials Park, OH, 2000.
- [7] R. Bud and D. J. Warner, *Instruments of science: an historical encyclopedia*, vol. 2. Taylor & Francis, 1998.
- [8] H. Kogelnik and T. Li, “Laser beams and resonators,” *Applied optics*, vol. 5, no. 10, pp. 1550–1567, 1966.
- [9] G. F. Marshall and G. E. Stutz, *Handbook of optical and laser scanning*. CRC Press, 2011.
- [10] N. McCormick and J. Lord, “Digital image correlation,” *Materials today*, vol. 13, no. 12, pp. 52–54, 2010.
- [11] S. Yoneyama and G. Murasawa, “Digital image correlation,” *Experimental Mechanics*. Eolss Publishers, 2009.
- [12] F. Hild and S. Roux, “Digital image correlation: from displacement measurement to identification of elastic properties—a review,” *Strain*, vol. 42, no. 2, pp. 69–80, 2006.
- [13] F. Hild and S. Roux, “Measuring stress intensity factors with a camera: Integrated digital image correlation (I-DIC),” *Comptes Rendus Mécanique*, vol. 334, no. 1, pp. 8–12, 2006.

- [14] S. Marth, H. Häggblad, M. Oldenburg, and R. Östlund, "Post necking characterisation for sheet metal materials using full field measurement," *Journal of Materials Processing Technology*, vol. 238, pp. 315–324, 2016.
- [15] K. S. Zhano and Z. H. Li, "Numerical analysis of the stress-strain curve and fracture initiation for ductile material," *Engineering fracture mechanics*, vol. 49, no. 2, pp. 235–241, 1994.
- [16] E. Fagerholt, *Field measurements in mechanical testing using close-range photogrammetry and digital image analysis*. PhD thesis, NTNU, 2012.
- [17] T. Kristensen, E. Fagerholt, and G. Gruben, "Edge tracing in tensile test using optical measurements," tech. rep., CASA - Departments of Structural Engineering, NTNU, 2016.
- [18] P. A. Schweitzer, *Metallic materials: physical, mechanical, and corrosion properties*, vol. 19. CRC Press, 2003.
- [19] O. S. Hopperstad and T. Børvik, "TKT4135 Materials Mechanics - Lecture notes," 2015.
- [20] T. L. Anderson, *Fracture mechanics: fundamentals and applications*. CRC press, 2005.
- [21] G. R. Johnson and W. H. Cook, "A constitutive model and data for metals subjected to large strains, high strain rates and high temperatures," in *Proceedings of the 7th International Symposium on Ballistics*, pp. 541–547, The Hague, The Netherlands, 1983.
- [22] T. Børvik, O. S. Hopperstad, T. Berstad, and M. Langseth, "A computational model of viscoplasticity and ductile damage for impact and penetration," *European Journal of Mechanics-A/Solids*, vol. 20, no. 5, pp. 685–712, 2001.
- [23] M. G. Cockcroft and D. J. Latham, "Ductility and the workability of metals," *J Inst Metals*, vol. 96, no. 1, pp. 33–39, 1968.
- [24] G. R. Johnson and W. H. Cook, "Fracture characteristics of three metals subjected to various strains, strain rates, temperatures and pressures," *Engineering fracture mechanics*, vol. 21, no. 1, pp. 31–48, 1985.
- [25] C. Bixby, *Nondestructive Evaluation and Quality Control*, vol. 17. ASM International, Materials Park, OH, 1989.
- [26] I. Westermann, K. O. Pedersen, T. Furu, T. Børvik, and O. S. Hopperstad, "Effects of particles and solutes on strength, work-hardening and ductile fracture of aluminium alloys," *Mechanics of Materials*, vol. 79, pp. pp. 58–72, 2014.
- [27] AEROEL, "Products Aeroal Laser Sensons & System for diameter control." <http://www.aeroel.it/products>. Obtained in March 2017.

- [28] B. Pan, K. Qian, H. Xie, and A. Asundi, “Two-dimensional digital image correlation for in-plane displacement and strain measurement: a review,” *Measurement science and technology*, vol. 20, no. 6, p. 062001, 2009.
- [29] J. Johnsen, J. K. Holmen, O. R. Myhr, O. S. Hopperstad, and T. Børvik, “A nano-scale material model applied in finite element analysis of aluminium plates under impact loading,” *Computational Materials Science*, vol. 79, pp. 724–735, 2013.
- [30] O. R. Myhr, Ø. Grong, and C. Schäfer, “An extended age-hardening model for Al-Mg-Si alloys incorporating the room-temperature storage and cold deformation process stages,” *Metallurgical and Materials Transactions A*, vol. 46, no. 12, pp. 6018–6039, 2015.
- [31] I. Westermann, K. O. Pedersen, T. Børvik, and O. S. Hopperstad, “Work-hardening and ductility of artificially aged AA6060 aluminium alloy,” *Mechanics of Materials*, vol. 97, pp. 100–117, 2016.
- [32] K. O. Pedersen, I. Westermann, T. Furu, T. Børvik, and O. S. Hopperstad, “Influence of microstructure on work-hardening and ductile fracture of aluminium alloys,” *Materials & Design*, vol. 70, pp. 31–44, 2015.
- [33] SNL, “Elektronmikroskop - Store norske leksikon.” <https://snl.no/elektronmikroskop>. Obtained in March 2017.
- [34] D. C. Joy, *Scanning electron microscopy*. Wiley Online Library, 2006.
- [35] E. Fagerholt, 2017. Private communication.
- [36] NDLA, “Skyvelære - teknikk og industriell produksjon.” <http://ndla.no/nb/node/50921?fag=35>. Obtained in March 2017.
- [37] LS-OPT, “Livermore Software Technology Corp.” <http://www.lstc.com/products/ls-opt>. Obtained in May 2017.
- [38] P. W. Bridgman, “The stress distribution at the neck of a tension specimen,” *Trans. ASM*, vol. 32, pp. 553–574, 1944.
- [39] G. Le Roy, J. D. Embury, G. Edwards, and M. F. Ashby, “A model of ductile fracture based on the nucleation and growth of voids,” *Acta Metallurgica*, vol. 29, no. 8, pp. 1509–1522, 1981.
- [40] Y. Bao, “Dependence of ductile crack formation in tensile tests on stress triaxiality, stress and strain ratios,” *Engineering fracture mechanics*, vol. 72, no. 4, pp. 505–522, 2005.
- [41] V. Vilamosa, A. H. Clausen, E. Fagerholt, O. S. Hopperstad, and T. Børvik, “Local measurement of stress–strain behaviour of ductile materials at elevated temperatures in a split-hopkinson tension bar system,” *Strain*, vol. 50, no. 3, pp. 223–235, 2014.
- [42] H. Granum, 2017. Private communication.

- [43] LS-DYNA, “Livermore Software Technology Corp.” <http://www.lstc.com>. Obtained in May 2017.
- [44] N. Stander, W. Roux, T. Eggleston, T. Goel, and K. Craig, “LS-OPT Version 5.2 Users Manual,” *Livermore Software Technology Corporation, Livermore*, 2015.
- [45] E. Fagerholt, D. Morin, T. Børvik, and O. S. Hopperstad, “DIC-based FEM: A coupled approach for investigation, validation and optimization of material models.” unpublished, 2016.
- [46] T. Børvik, 2017. Private communication.

A | Appendix

A.1 Initial Dimensions of the Tensile Specimens

The diameters in Table A.1 are measured with the AEROEL XLS 13XY laser micrometer in two directions. The dimensions in Tables A.2 and A.3 are measured with a digital slide gauge.

Table A.1: Measured diameters of the round specimens with 5 mm gauge length used in the tension tests with laser. Measures in mm.

Test No.	$D_{1,0}$	$D_{2,0}$
1	2.9642	2.9646
2	2.9431	2.9435
3	2.9498	2.9499

Table A.2: Measured diameters of the round specimens used in the tension test with edge tracing. Measures in mm. Nom. = nominal value.

Geometry	Test No.	D_0
Round L5	1	3.000 (Nom.)
	2	3.000 (Nom.)
	3	3.000 (Nom.)
	4	2.970
Round L40	1	6.003
	2	6.003
	3	6.002
	4	6.007

Table A.3: *Measured thickness and width of the flat specimens. Measures in mm.*

Geometry	Test No.	t_0	b_0
Flat L20	1	3.01	4.91
	2	2.99	4.90
	3	3.03	4.87
	4	2.99	4.93
Flat L50	1	3.015	12.30
	2	3.00	12.28
	3	3.04	12.39
	4	3.02	12.40

A.2 Nominal Dimensions of the Component

The nominal dimensions for the rectangular tube used in the numerical case study is given in Figure A.1.

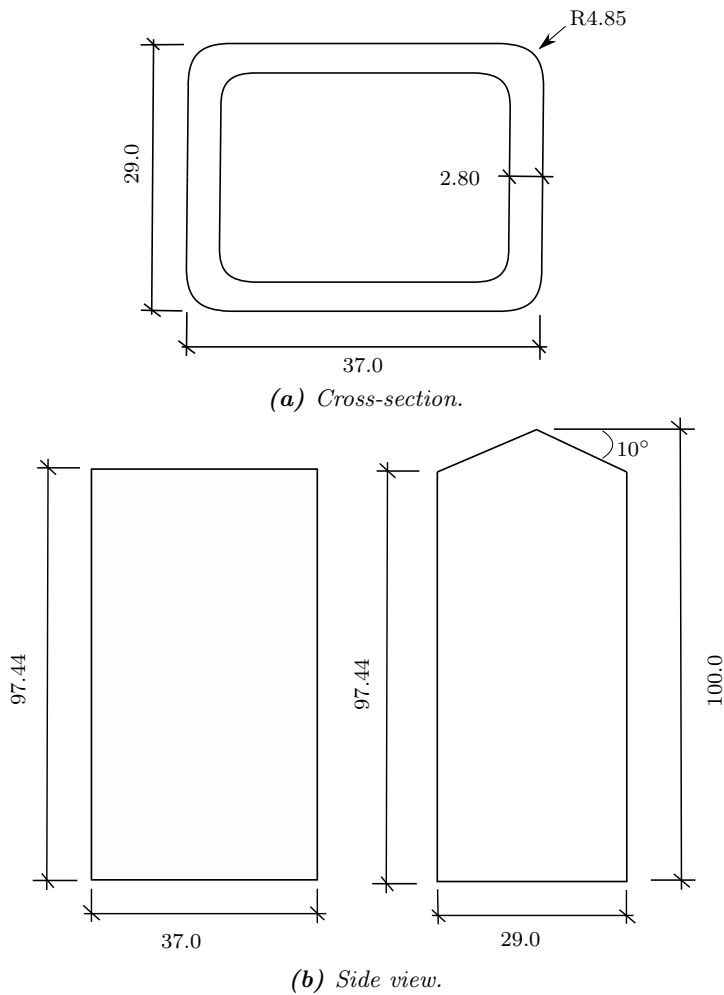


Figure A.1: The nominal dimensions of the rectangular tube. Measures in mm.